MJO Propagation over the Indian Ocean and Western Pacific in CMIP5 Models: Roles of Background States

GUIWAN CHEN,[a,b] JIAN LING,[a,b] YUANWEN ZHANG,[a,b] XIN WANG,[c,d,e] and CHONGYIN LI[a]

[a] *State Key Laboratory of Numerical Modelling for Atmospheric Sciences and Geophysical Fluid Dynamics, Institute of Atmospheric Physics, Chinese Academy of Sciences, Beijing, China*
[b] *University of Chinese Academy of Sciences, Beijing, China*
[c] *State Key Laboratory of Tropical Oceanography, South China Sea Institute of Oceanology, Chinese Academy of Sciences, Guangzhou, China*
[d] *Southern Marine Science and Engineering Guangdong Laboratory (Guangzhou), Guangzhou, China*
[e] *Innovation Academy of South China Sea Ecology and Environmental Engineering, Chinese Academy of Sciences, Guangzhou, China*

(Manuscript received 31 March 2021, in final form 14 October 2021)

ABSTRACT: This study explores the impacts of background states on the propagation of the Madden–Julian oscillation (MJO) in 24 CMIP5 models using a precipitation-based MJO tracking method. The ability of the model to reproduce the MJO propagation is reflected in the occurrence frequency of individual MJO events. Moisture budget analysis suggests that the occurrence frequencies of MJO events that propagate across the Indian Ocean (IO-MJO) and western Pacific (WP-MJO) in the models are mainly related to the low-level meridional moisture advection ahead of the MJO convection center. This advection is tightly associated with the background distribution of low-level moisture. Drier biases in background low-level moisture over the entire tropical regions account for underestimated MJO occurrence frequency in the bottom-tier simulations. This study highlights the importance of reproducing the year-to-year background states for the simulations of MJO propagation in the models by further decomposing the background states into the climatology and anomaly components. The background meridional moisture gradient accounting for the IO-MJO occurrence frequency is closely related to its climatology component; however, the anomaly component regulated by El Niño–Southern Oscillation (ENSO) is also important for the WP-MJO occurrence frequency. The year-to-year variations of background zonal and meridional gradients associated with ENSO account for the IO-MJO occurrence frequency tend to be offset from each other. As a result, ENSO shows no significant impact on the IO-MJO occurrence frequency. However, the MJO events are more likely to propagate across the western Pacific during El Niño years.

KEYWORDS: Madden–Julian Oscillation; Model comparison; Interannual variability; Intraseasonal variability; Moisture/moisture budget

1. Introduction

The Madden–Julian oscillation (MJO; Madden and Julian 1971, 1972) is one of the dominant modes of the intraseasonal variability in the tropical atmosphere. The MJO is characterized by slowly eastward-propagating (~5 m s^{-1}) circulation–convection coupled systems at a planetary scale. Its convection usually starts over the Indian Ocean and terminates over the central Pacific where the sea surface temperatures (SSTs) are cold (Zhang 2005). The MJO plays an important role in bridging weather and climate (Zhang 2013; Li et al. 2020) and therefore represents one of the primary sources of predictability for extended-range weather prediction [see review in Kim et al. (2018)].

However, the simulation of the MJO in the state-of-the-art general circulation models remains a challenge; most models still cannot realistically reproduce the MJO, especially its eastward propagation (Jia et al. 2008; Ling et al. 2009; Hung et al. 2013; Jiang et al. 2015; Ahn et al. 2020). Hung et al. (2013) found that among the 20 models participating in phase 5 of the Coupled Model Intercomparison Project (CMIP5), only one (CNRM-CM5) can simulate the eastward propagation of MJO. Of the 27 models participating in the MJO Task Force (MJOTF) and the Global Energy and Water Cycle Experiment (GEWEX) Atmospheric System Study (GASS) (MJOTF/GASS) project, only about 8 can reproduce reasonable eastward propagation of the large-scale convection associated with the MJO (Jiang et al. 2015). It has been reported that, due to improved low-level moisture distribution, the MJO propagation over the Maritime Continent is improved in models participating in phase 6 of the Coupled Model Intercomparison Project (CMIP6) when compared with the CMIP5 models (Ahn et al. 2020). However, the general propagation characteristics of the MJO are still underestimated by the majority of CMIP6 models. Compared with observations, the MJO events in the models tend to be more likely to be blocked by the Maritime Continent (Inness and Slingo 2003; Kim et al. 2009; Ling et al. 2019; Chen et al. 2020). The inability to reproduce the eastward propagation of the MJO in the models could be due to the exaggerated barrier effect on the MJO propagation over the Maritime Continent (Ling et al. 2019; Chen et al. 2020).

Biases in the background states of the models are often blamed for the inability of models to reproduce the MJO, such as the cold bias in the tropical SST (Inness et al. 2003; Sperber 2004; Seo et al. 2007) and dry biases in the low-level

Corresponding author: Jian Ling, lingjian@lasg.iap.ac.cn

DOI: 10.1175/JCLI-D-21-0255.1

moisture over the Maritime Continent (Gonzalez and Jiang 2017). By introducing a flux-corrected experiment using the Hadley Centre model (HadCM3), Inness et al. (2003) found that the cold bias in SST over the warm pool and the mean near-equatorial easterly wind errors were reduced, corresponding with stronger MJO eastward propagation. Using the National Centers for Environmental Prediction Coupled Forecasting System (CFS), Seo et al. (2007) also found that its flux-corrected version simulated stronger MJO propagation due to warmer mean SST, stronger low-level equatorial westerlies, and stronger wind shear. Cold SST bias over the equatorial western Pacific is a long-standing problem in the coupled models, known as the excessive equatorial cold tongue bias (Li and Xie 2014). It is worth investigating whether the poor simulations of the MJO propagation by multimodel ensembles is related to the cold SST bias over the equatorial Pacific. Under the framework of the "moisture mode" theory of the MJO, numerous studies have documented the importance of background states in low-level moisture for the MJO. It has been reported that the drier biases in the lower troposphere over the tropical region are the main reason for models failing to reproduce the MJO (Gonzalez and Jiang 2017; Kim 2017; Kang et al. 2020). The drier low-level troposphere over the tropics reduces the meridional moisture gradient, hence reducing the meridional moisture advection that is important for the MJO propagation.

When investigating the impacts of background states on the statistical signals of the MJO, most previous studies have focused on the climatology of the models. Recently, a new method for diagnosing the MJO simulation has been proposed (Ling et al. 2014, 2017; Zhang and Ling 2017; Ling et al. 2019; Chen et al. 2020). In this method, the propagation characteristics of the individual MJO events identified in each model are compared, instead of comparing the MJO statistical signals (e.g., spectrum analysis and lag-regression analysis). Based on the MJO events identified by tracking the eastward propagation of positive equatorial precipitation anomalies using MJOTF/GASS models, Ling et al. (2017) found that all the models examined can produce the MJO events regardless of their ability to reproduce the MJO statistical signals. The difference is that some models produce MJO events more frequently than others. They further proposed that the year-to-year background states in the models determine the occurrence frequencies of the MJO events they reproduced. The MJO can be reproduced only under certain background states; models produce MJO events more frequently if they are constantly under background states that are favorable for reproducing the MJO. Thus, it is necessary to explore the impacts of the background states, which are determined mainly by the climatology and interannual variabilities of the model, on the MJO propagation in the models.

The year-to-year background states over the tropics are most relevant to El Niño–Southern Oscillation (ENSO). As the dominant mode of the interannual variabilities over the Pacific Ocean, ENSO has significant impacts on MJO activity. During the mature phase of El Niño, the MJO is more active over the central Pacific due to the warmer SST there, but its intensity is weaker over the Indian Ocean (F. Liu et al. 2016; Wu and Song 2018) and the Maritime Continent (Liu et al. 2020). More MJO events tend to propagate farther eastward into the eastern Pacific during El Niño years (Li and Smith 1995; Tam and Lau 2005). ENSO could also significantly influence the MJO propagation speed (Wei and Ren 2019; B. Wang et al. 2019; Chen and Wang 2020). During the El Niño phase, the phase speed of the MJO is faster due to the enhancement of low-level premoistening ahead of the MJO convection induced by the warmer SST. Klingaman and Demott (2020) suggested that the year-to-year background states related to ENSO have an impact on the MJO simulation by modulating the air–sea coupling processes.

This study explored the potential impacts of background states on the MJO propagation over the Indian Ocean and western Pacific in 24 CMIP5 historical simulations. The objective of this study is to explore the roles of background states on MJO propagation in CMIP5 models, including the climatology and interannual variabilities of background states. Most previous studies have focused on MJO propagation over the Indian Ocean, as most MJO events start over this region. However, the MJO propagation over the western Pacific is also important, as whether the MJO can propagate into this region leads to different impacts of the MJO on global weather and climate (Li et al. 2020). As such, this study tried to compare the impacts of background states on the MJO propagation over the Indian Ocean and the western Pacific. The annual occurrence frequency of individual MJO events obtained from a precipitation-based MJO tracking method was used to quantitatively evaluate how well the models can reproduce the MJO propagation. Moisture budget analysis was applied to compare the moisture transport processes ahead of the MJO convection between models that produce MJO events more frequently and less frequently. The impacts of background states and their interannual variabilities associated with ENSO on the MJO were further analyzed. The remainder of this paper is structured as follows. In section 2, we introduce the models diagnosed, the observational datasets, and the methods used in this study. The results are presented in section 3. A summary and discussion are presented in section 4.

2. Data and method

a. *Models and validation datasets*

Daily outputs from historical simulations in 24 CMIP5 models (Table 1; Taylor et al. 2012) were diagnosed in this study, covering the period of 1950–2005. Multiple observational datasets covering a shorter period, from 1979 to 2015, were used for validation. Pentad mean Climate Prediction Center (CPC) Merged Analysis of Precipitation (CMAP) rainfall (Xie and Arkin 1997) was used to identify individual MJO events in observations. The SST dataset used was the monthly mean Hadley Centre Global Sea Ice and Sea Surface Temperature (HadISST; Rayner et al. 2003), with a horizontal

TABLE 1. CMIP5 models used in this study. (Expansions of many acronyms are available online at http://www.ametsoc.org/PubsAcronymList.)

Model	Institute	Spatial resolution (lon × lat)
ACCESS1.0	CSIRO and BOM, Australia	1.875° × 1.25°
ACCESS1.3	CSIRO and BOM, Australia	1.875° × 1.25°
CanESM2	CCCma, Canada	2.81° × 2.79°
CMCC-CESM	CMCC, Italy	3.75° × 3.44°
CMCC-CM	CMCC, Italy	0.75° × 0.75°
CMCC-CMS	CMCC, Italy	3.75° × 3.71°
CNRM-CM5	CNRM and CERFACS, France	1.41° × 1.40°
FGOALS-g2	IAP and THU, China	2.81° × 2.79°
FGOALS-s2	IAP, China	2.81° × 1.66°
GFDL-CM3	NOAA GFDL, United States	2.5° × 2.0°
GFDL-ESM2G	NOAA GFDL, United States	2.5° × 2.0°
IPSL-CM5A-LR	IPSL, France	3.75° × 1.89°
IPSL-CM5A-MR	IPSL, France	2.5° × 1.27°
IPSL-CM5B-LR	IPSL, France	3.75° × 1.89°
MIROC4h	AORI, NIES, JAMSTEC, Japan	0.56° × 0.56°
MIROC5	AORI, NIES, JAMSTEC, Japan	1.41° × 1.40°
MIROC-ESM	AORI, NIES, JAMSTEC, Japan	2.81° × 2.79°
MIROC-ESM-CHEM	AORI, NIES, JAMSTEC, Japan	2.81° × 2.79°
MPI-ESM-LR	MPI, Germany	1.875° × 1.87°
MPI-ESM-MR	MPI, Germany	1.875° × 1.87°
MPI-ESM-P	MPI, Germany	1.875° × 1.87°
MRI-CGCM3	MRI, Japan	1.125° × 1.12°
MRI-ESM1	MRI, Japan	1.125° × 1.12°
NorESM1-M	Norwegian Climate Centre	2.5° × 1.89°

resolution of 1° × 1°. The daily specific humidity and three-dimensional wind components (0.75° × 0.75°) used were from the European Centre for Medium-Range Weather Forecasts interim reanalysis (ERA-Interim; Dee et al. 2011).

All the simulation outputs and the observational datasets were interpolated into the same horizontal grids (2.5° × 2.5°). The pentad CMAP data were interpolated to daily resolution before tracking the MJO. This study focused on the periods during the extended boreal winter (October–March) when the eastward propagation of the MJO is distinct.

b. Method

Individual MJO events were identified by tracking the eastward propagating large-scale positive precipitation anomalies in the tropics (Ling et al. 2014; Zhang and Ling 2017). Before tracking the MJO, the tropical precipitation anomalies were obtained by first removing the climatological seasonal cycle and then averaging between 15°S and 15°N. A two-dimensional time–space fast Fourier transform was then applied to extract the large-scale (zonal wavenumbers 0–6) and intraseasonal (20–100 days) signals to represent the MJO (Wheeler and Kiladis 1999). Both eastward and westward propagating signals were retained. It is a common practice to retain only the eastward propagating signals when subtracting the observational MJO signals (Gottschalck et al. 2013; Zhang and Ling 2017), as they clearly dominate the intraseasonal band in observations (Zhang and Hendon 1997). However, in the simulations, retaining only the eastward signals would overestimate the MJO signals because the westward propagating signals can be as strong as or even stronger than the eastward propagating signals (Zhang et al. 2006; Jiang et al. 2015). The MJO tracking method of Zhang and Ling (2017) was applied to the filtered precipitation anomalies to objectively identify the eastward propagating large-scale precipitation envelopes. Those large-scale precipitation envelopes that propagate eastward for at least 50° in longitude at a speed of 3–7 m s^{-1} with a time interval longer than 20 days were treated as MJO events. The eastward propagation of the MJO is allowed to break down over a distance no longer than 10° in longitude, as described in Zhang and Ling (2017). This MJO tracking method provides specific quantities that measure the characteristics (e.g., starting and ending longitudes, speed, strength, propagating ranges, and life spans) of individual MJO events, which are not available from the empirical orthogonal function (EOF)-based MJO indices (Wheeler and Hendon 2004; Straub 2013; P. Liu et al. 2016).

The Student's t test was applied to assess the significance of the composited results and linear correlation coefficients. Composites of wind vector are considered significant if either one component passes the Student's t test. The word "significant" is used in this study only if results pass the test at the 95% confidence level.

3. Results

a. MJO simulation ability

All CMIP5 simulations diagnosed in this study produce MJO events represented by eastward propagating large-scale

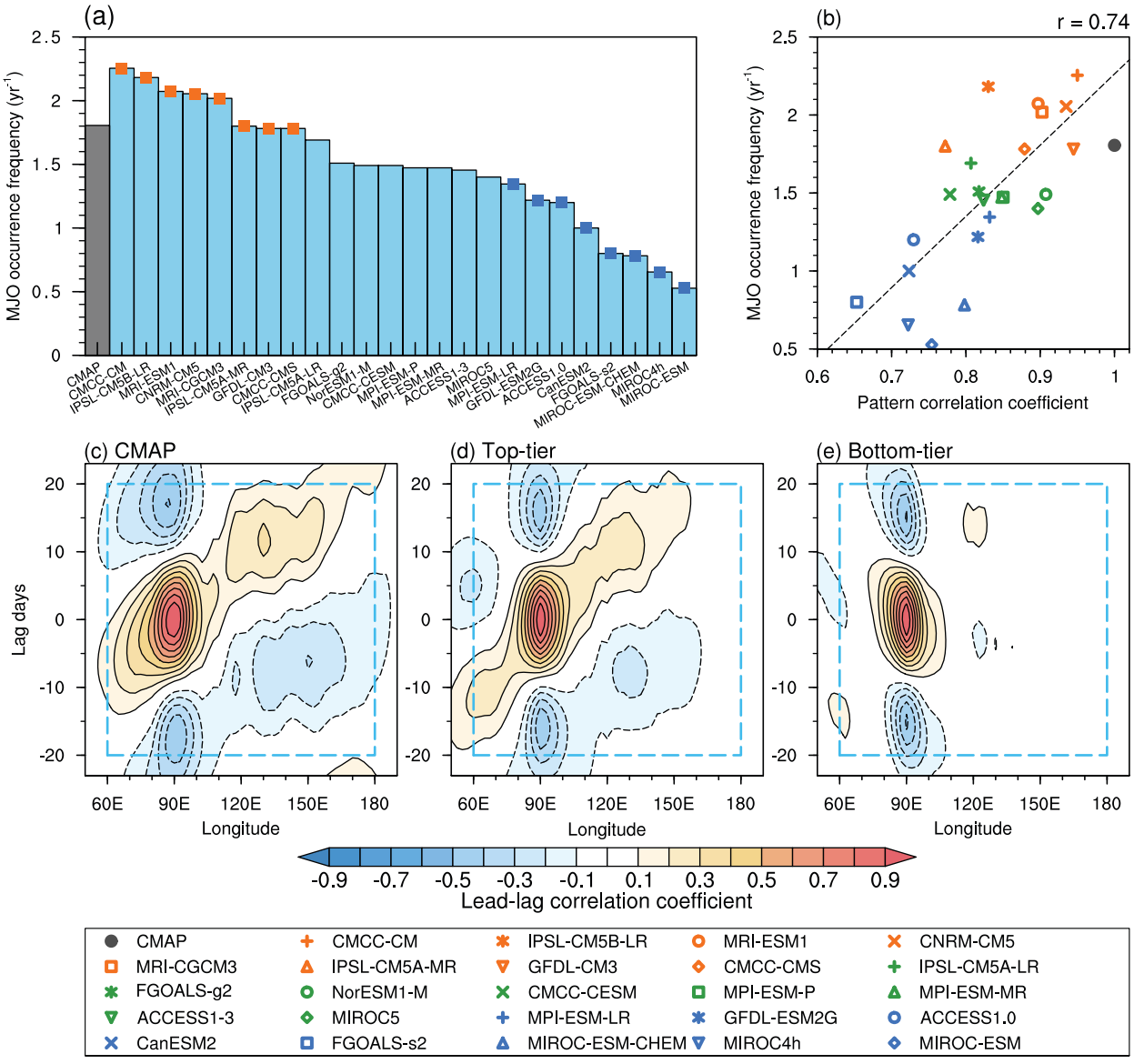

FIG. 1. (a) Bar plots of occurrence frequencies (yr^{-1}) of identified MJO events over the tropics in CMAP (gray bar) and 24 CMIP5 simulations (light blue bars). (b) Scatterplots of occurrence frequencies of identified MJO events over the tropics vs the pattern correlation coefficient metrics for CMAP and the simulations. Also shown are lead–lag correlation coefficient of 20–100-day bandpass filtered equatorial averaged (15°S–15°N) precipitation anomalies at each longitude with that at 90°E in (c) CMAP, (d) top-tier, and (e) bottom-tier simulations. The orange and blue squares in (a) mark the top- and bottom-tier simulations, respectively. The pattern correlation coefficient metrics in (b) are calculated as the pattern correlation of the lead-lag correlation coefficient from day −20 to day 20 over 60°E–180° between each simulation and CMAP as indicated by the blue dashed box.

precipitation anomalies over the tracking domain spanning eastward from 40° to 120°W (Fig. 1a). However, around two-thirds of the simulations underestimate the MJO occurrence frequency, so MJO simulation remains a challenge in most models. The annual occurrence frequency of the MJO is used to quantitatively evaluate the ability of the models to simulate the MJO. As will be demonstrated later, this metric can represent the ability of the models to reproduce the statistical signals of the MJO propagation. Based on this metric, eight simulations with the highest MJO occurrence frequency were grouped as the top-tier simulations (marked by orange squares in Fig. 1a), while another eight simulations with the lowest MJO occurrence frequency were grouped as the bottom-tier simulations (marked by blue squares in Fig. 1a). This study focused on the comparisons between the top- and bottom-tier simulations, through which factors that possibly determine a model's ability to reproduce the MJO propagation can be revealed.

Evidence of the MJO in observations is the robust eastward propagation of its precipitation from the Indian Ocean to the Pacific Ocean in lead–lag correlation diagrams of tropical precipitation anomalies (Fig. 1c). This feature is reproduced well by the top-tier simulations (Fig. 1d), but the precipitation anomalies exhibit stationary oscillation over the Indian Ocean in the bottom-tier simulations (Fig. 1e). This suggests that the top-tier simulations can reproduce the MJO statistical signals, but the bottom-tier simulations cannot. To quantitatively represent the capabilities of the models to reproduce the MJO statistical signals, the pattern correlation coefficient (PCC) between the lead–lag correlation patterns of precipitation in the range 60°E–180° and from day −20 to day 20 (blue dashed rectangles in Figs. 1c–e) in observations and each individual simulation were calculated. This metric has been widely adapted in MJO diagnosis (Jiang et al. 2015; Ling et al. 2017; Wang et al. 2018). A PCC value close to 1 suggests that the model-produced MJO propagation signal is close to the observation, while a smaller PCC value suggests that the MJO eastward propagation in the models is not distinct. There was significant correlation between the annual occurrence frequency of identified MJO events and the PCC metric among the simulations (Fig. 1b). This result confirms that the occurrence frequency of model-produced MJO events can be used to indicate the ability of the model to simulate the MJO propagation.

b. *Low-level moisture budget analysis*

In this study, the MJO propagation characteristics over both the Indian Ocean and western Pacific were investigated. The MJO events that propagate across 90°E (initiating west of 90°E and terminating east of 90°E) are grouped as the Indian Ocean MJO (IO-MJO) events. Similarly, those that propagate across 150°E (initiating west of 150°E and terminating east of 150°E) are identified as the western Pacific MJO (WP-MJO) events. Day 0 is defined as the time when the MJO convection center passes through 90°E for IO-MJO events and 150°E for WP-MJO events. It should be noted that some MJO events are grouped into both the IO-MJO and WP-MJO categories if their convection center starts west of 90°E and terminates east of 150°E. The aim of this study was not to directly compare IO-MJO and WP-MJO; we aimed to explore the simulated MJO propagation over the Indian Ocean and western Pacific by diagnosing possible factors that regulate the occurrence frequency of IO-MJO and WP-MJO events. As the tracking procedure requires that the MJO convection center propagates eastward for at least 50° in longitude, the occurrence frequencies of identified IO-MJO and WP-MJO events in the models indicate how well the models can reproduce the MJO propagation over the Indian Ocean and western Pacific.

There is distinct eastward propagation in precipitation for IO-MJO and WP-MJO events in observations as well as the top- and the bottom-tier simulations (contours in Fig. 2). However, the eastward propagation range in longitude is shorter in the simulations, especially in the bottom-tier simulations, when compared with the observations. The distinct eastward propagation in precipitation from the Indian Ocean to the central Pacific for both IO-MJO and WP-MJO events is clear in observations (Figs. 2a,d) but the eastward propagation signals of IO-MJO events disappear around 140°E and the WP-MJO events mainly originate over the Maritime Continent in the bottom-tier simulations (Figs. 2c,f). An eastward propagating positive low-level (1000–700-hPa weight averaged) moisture tendency anomaly leading the MJO convection is clear in observations and the simulations (shading in Fig. 2) for both IO-MJO and WP-MJO events. However, compared with the observations and the top-tier simulations, the low-level moisture tendency ahead of the MJO convection center in the bottom-tier simulations is weaker and propagates over a shorter range.

Figure 3 shows the composited vertical-zonal structures of IO-MJO and WP-MJO events averaged from day −15 to day −5 as indicated by the black rectangles in Fig. 2. The time period from day −15 to day −5 was chosen to explore precursor factors that may determine the occurrence frequency of IO-MJO and WP-MJO events. At this time, the convection is active over the western Indian Ocean for IO-MJO and over the Maritime Continent for WP-MJO (curves in Fig. 3). Both the IO-MJO and WP-MJO events identified in the top- and bottom-tier simulations exhibit the conventional vertical–zonal structures of the MJO (Fig. 3). There are easterlies (westerlies) to the east (west) of MJO convection centers at lower levels and a reversed phase at upper levels; the westward-tilt structure in moisture is also obvious. The structures of the MJO events identified in the top-tier simulations are closer to those in the observations (Fig. 3b); however, in the bottom-tier simulations, both the active and suppressed convective centers quantified by the precipitation of MJO events are weaker than the observed. This is an indicator of weaker MJO in the bottom-tier simulations that has been documented by Chen et al. (2020). Consistently, the MJO events in the bottom-tier simulations exhibit weaker moisture and circulations anomalies. The low-level easterlies ahead of the MJO convection centers are weaker in the bottom-tier simulations. Low-level premoistening ahead of the MJO convection centers over the Indian Ocean for IO-MJO and western Pacific for WP-MJO is also weaker, and this may account for the shorter propagation range of MJO events in the bottom-tier simulations (Hsu et al. 2014).

From day −15 to day −5, a positive low-level moisture tendency is obvious ahead of the convection of IO-MJO and WP-MJO events in both observations and the simulations (Fig. 4). This positive low-level moisture tendency is important for the premoistening processes ahead of the MJO convection centers that promote the eastward propagation of the MJO (Hsu and Li 2012). The bottom-tier simulations underestimate the low-level moisture tendency ahead of the MJO convection for IO-MJO and WP-MJO events (Fig. 4). The low-level moisture budget analysis ahead of the MJO convection center (indicated by black rectangles in Fig. 4) from day −15 to day −5 was applied for both IO-MJO and WP-MJO

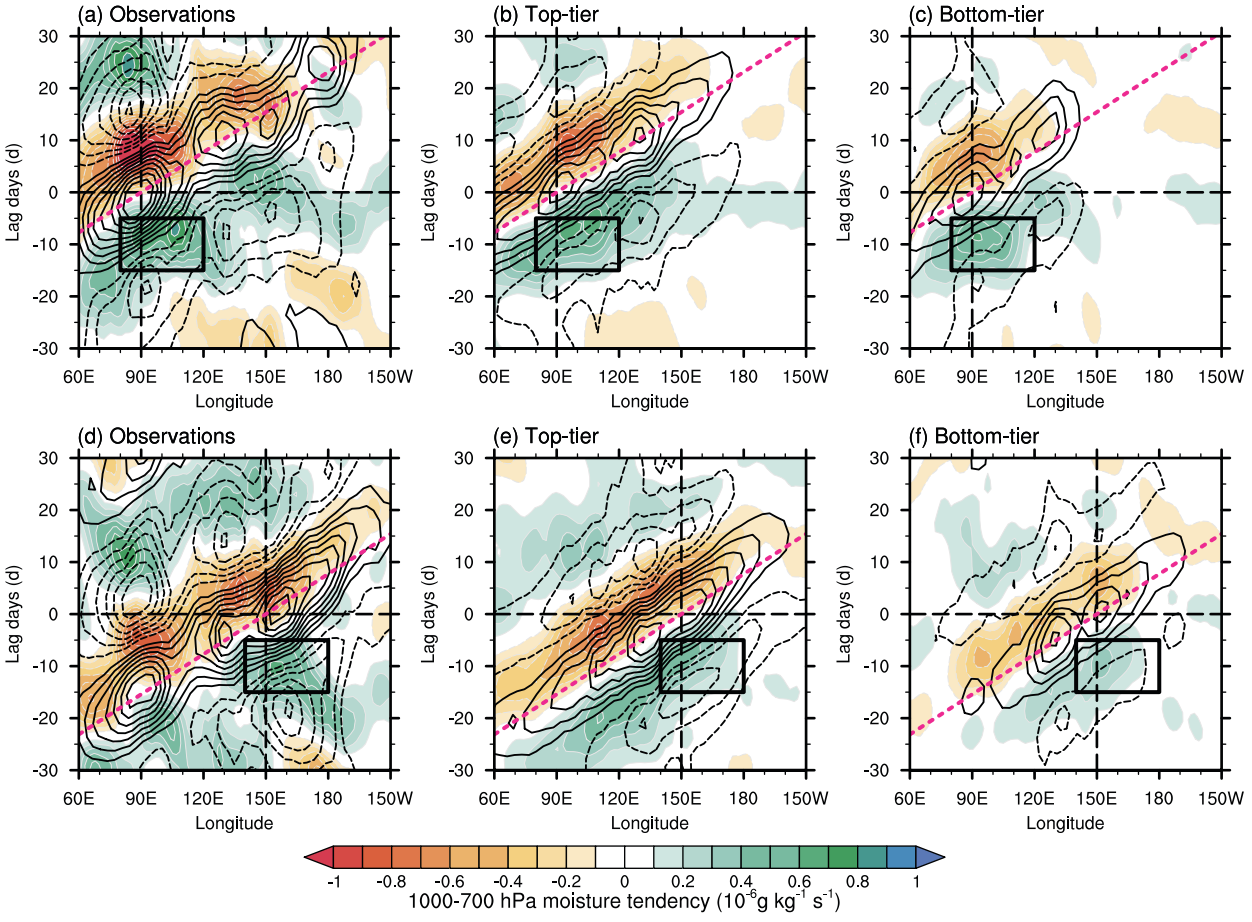

FIG. 2. Composites of time–longitude evolutions of 20–100-day bandpass filtered precipitation anomalies (contour; interval: 0.5 mm day^{-1}) and 1000–700-hPa weight-averaged moisture tendency (shading; 10^{-6} g kg^{-1} s^{-1}) for identified (a)–(c) IO-MJO and (d)–(f) WP-MJO events in the (left) observations, (center) top-tier simulations, and (right) bottom-tier simulations over the tropics (15°S–15°N). The black horizontal dashed lines mark day 0 when the MJO convection centers pass through 90° and 150°E for IO-MJO and WP-MJO events, respectively. The black vertical dashed lines mark 90°E for IO-MJO and 150°E for WP-MJO, respectively; the magenta dashed lines make the eastward propagation speed of 5 m s^{-1}. The rectangles mark the regions ahead of the MJO convection centers of 80°–120°E for IO-MJO and 140°E–180° for WP-MJO from day −15 to day −5.

events in both observations and the simulations, following Yanai et al. (1973):

$$\frac{\partial q}{\partial t} = -u\frac{\partial q}{\partial x} - v\frac{\partial q}{\partial y} - \omega\frac{\partial q}{\partial p} - \frac{Q_2}{L}, \tag{1}$$

where u, v, and ω denote three-dimensional wind components; q denotes the specific humidity; Q_2 represents the apparent moisture sink/source that related to the combined processes of precipitation, evaporation, and moisture fluxed by microphysical processes; and L denotes the latent heat of condensation. There is no explicit representation of the $-Q_2/L$ term in the ERA-Interim reanalysis; it was implicitly calculated as the residual term from the sum of other terms. Previous studies have suggested that the vertical moisture advection ($-\omega\partial q/\partial p$) is mostly canceled by the moisture sink/source $-Q_2/L$ (Kiranmayi and Maloney 2011; Adames and Wallace 2015), which is mainly determined by the condensation in regions of ascent (Adames and Wallace 2015). Hence, they are treated as the column processes in this study.

Both the top- and bottom-tier simulations underestimate the low-level moisture tendency ahead of the MJO convection center for IO-MJO and WP-MJO events (Fig. 5), especially for the bottom-tier simulations. The low-level moisture tendency is mainly dominated by the meridional moisture advection for both IO-MJO and WP-MJO events. For IO-MJO events, the contribution from the zonal moisture advection is nonnegligible but much smaller than the meridional component (Fig. 5a), while it is negligible for WP-MJO events (Fig. 5b). This is consistent with previous results that suggest the difference in moisture advection processes for the MJO over the Indian Ocean and the western Pacific (Hsu and Li 2012). Stronger meridional moisture advection in top-tier simulations than in the bottom-tier simulations explains their

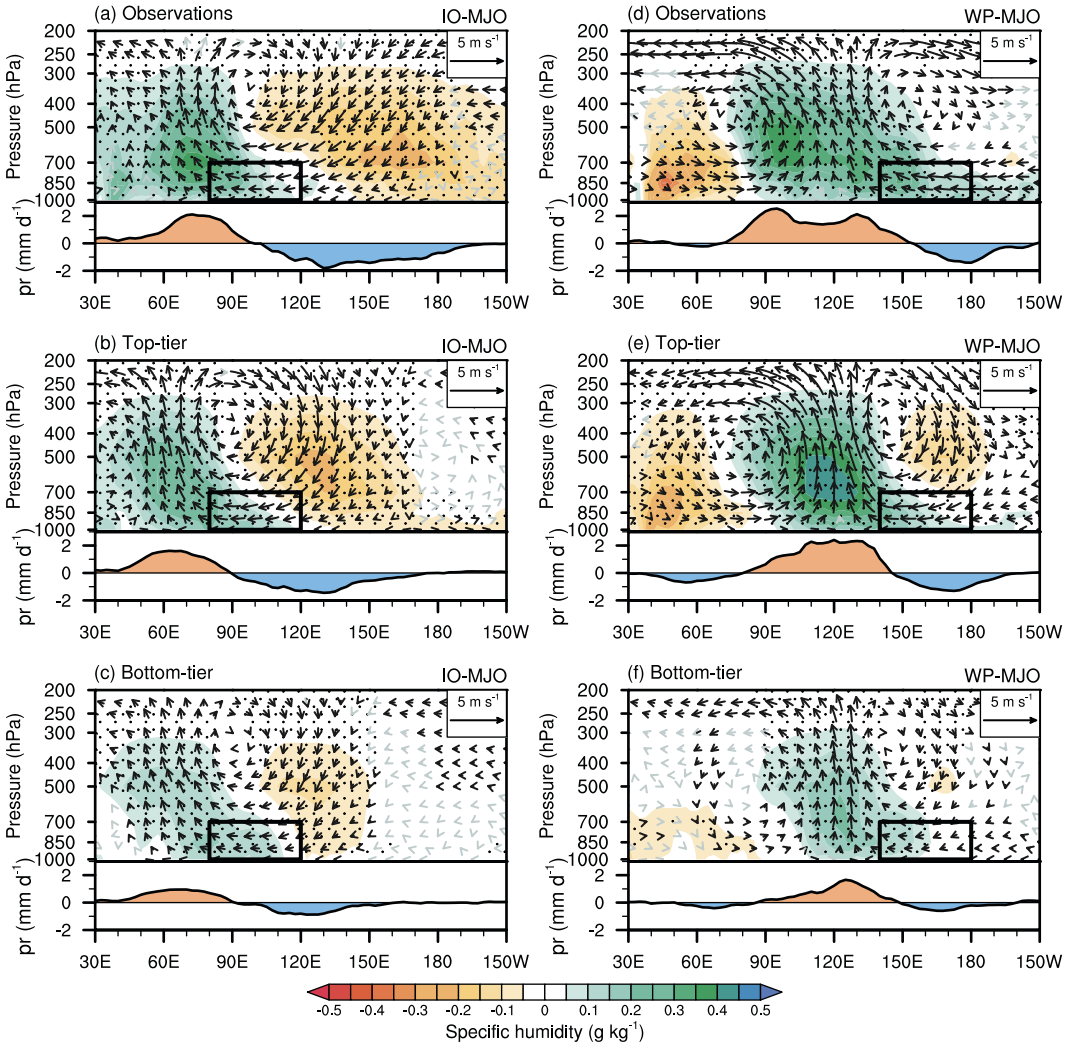

FIG. 3. Vertical–zonal distributions of composites of equatorial averaged (15°S–15°N) 20–100-day bandpass filtered anomalous specific humidity (shading; g kg^{-1}) and u–ω wind (vectors) as well as corresponding equatorial averaged filtered precipitation anomalies (curves; mm day^{-1}) for (a)–(c) IO-MJO and (d)–(f) WP-MJO events in the (top) observations, (middle) top-tier simulations, and (bottom) bottom-tier simulations averaged between day −15 and day −5. Vertical velocities are scaled by a factor of 100 to make them visible. Results significant at the 95% confidence level are marked by black arrows for wind vectors and by stippling for specific humidity. The black rectangles mark the regions of 80°–120°E for IO-MJO and 140°E–180° for WP-MJO between 1000 and 700 hPa.

differences in moisture tendency (Fig. 4), which can further explain their differences in the occurrence frequencies of IO-MJO and WP-MJO events.

The meridional moisture advection term ($-v\partial q/\partial y$) is much larger in the top-tier simulations for both IO-MJO and WP-MJO events when compared with the observations and the bottom-tier simulations (Fig. 5). This might be the result of error compensation. To explore possible reasons for the larger meridional moisture advection in the top-tier simulations, this term was further evaluated through a scale decomposition analysis. Following Hsu and Li (2012), the specific humidity and meridional velocity were decomposed into the low-frequency background states (LFBS; with a period beyond 100 days), the intraseasonal components (with a period between 20 and 100 days), and the high-frequency components (with a period within 20 days):

$$q = \overline{q} + q' + q^*; \quad v = \overline{v} + v' + v^*, \tag{2}$$

where the bar, prime, and asterisk denote LFBS, intraseasonal, and high-frequency components, respectively. Based on this decomposition, the meridional moisture advection term can be further divided into nine terms:

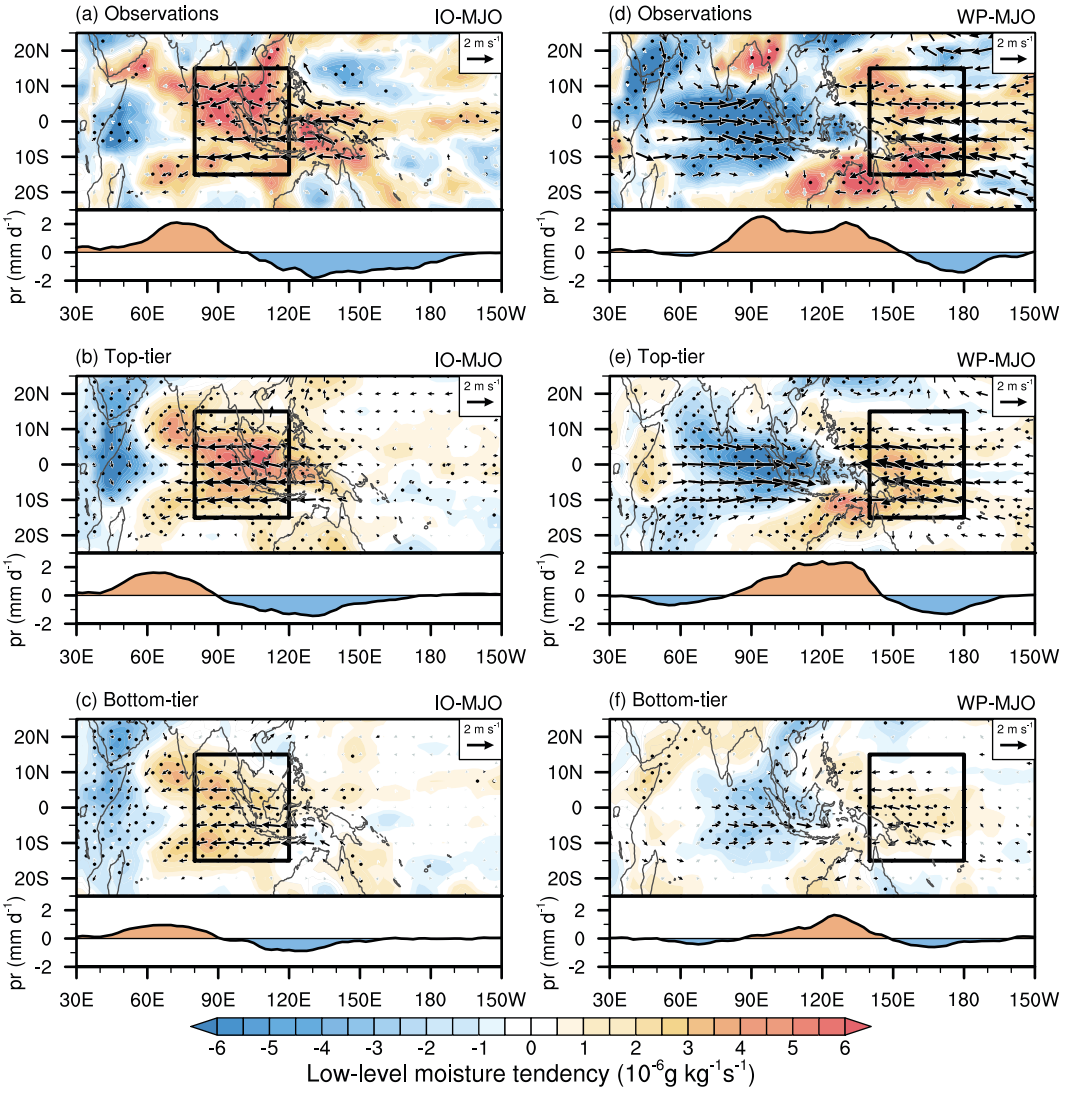

FIG. 4. Composites of 20–100-day bandpass filtered 1000–700-hPa weight-averaged moisture tendency (10^{-6} g kg^{-1} s^{-1}) and equatorial averaged (15°S–15°N) filtered precipitation anomalies (curves; mm day^{-1}) for (a)–(c) IO-MJO and (d)–(f) WP-MJO events in the (top) observations, (middle) top-tier simulations, and (bottom) bottom-tier simulations averaged between day −15 and day −5. Results significant at the 95% confidence level are marked by black arrows for wind vectors and by stippling for moisture tendency. The black rectangles mark the regions ahead of the MJO convection for IO-MJO (80°–120°E, 15°S–15°N) and WP-MJO events (140°E–180°, 15°S–15°N).

$$-v\frac{\partial q}{\partial y} = -\overline{v}\frac{\partial \overline{q}}{\partial y} - \overline{v}\frac{\partial q'}{\partial y} - \overline{v}\frac{\partial q^*}{\partial y} - v'\frac{\partial \overline{q}}{\partial y} - v'\frac{\partial q'}{\partial y} - v'\frac{\partial q^*}{\partial y} - v^*\frac{\partial \overline{q}}{\partial y} - v^*\frac{\partial q'}{\partial y} - v^*\frac{\partial q^*}{\partial y}. \quad (3)$$

The meridional moisture advection is mainly attributed to the advection of LFBS specific humidity by the intraseasonal meridional wind for both IO-MJO and WP-MJO events in observations, the top- and bottom-tier simulations (Fig. 6). The contribution of the advection of the high-frequency specific humidity by the high-frequency meridional wind is also nonnegligible. This term is induced by the synoptic-scale eddies due to the MJO-perturbed wind anomalies via barotropic energy conversion (Maloney 2009), which might indicate that the extratropical influence of synoptic disturbances on the MJO is also important (Zhao et al. 2013; Pang et al. 2018). The weaker meridional moisture advection in the bottom-tier simulations compared with the top-tier simulations can be mainly explained by their differences in the advection of LFBS specific humidity by the intraseasonal meridional wind (Fig. 6). This suggests that the background specific humidity in the models may play important roles in MJO

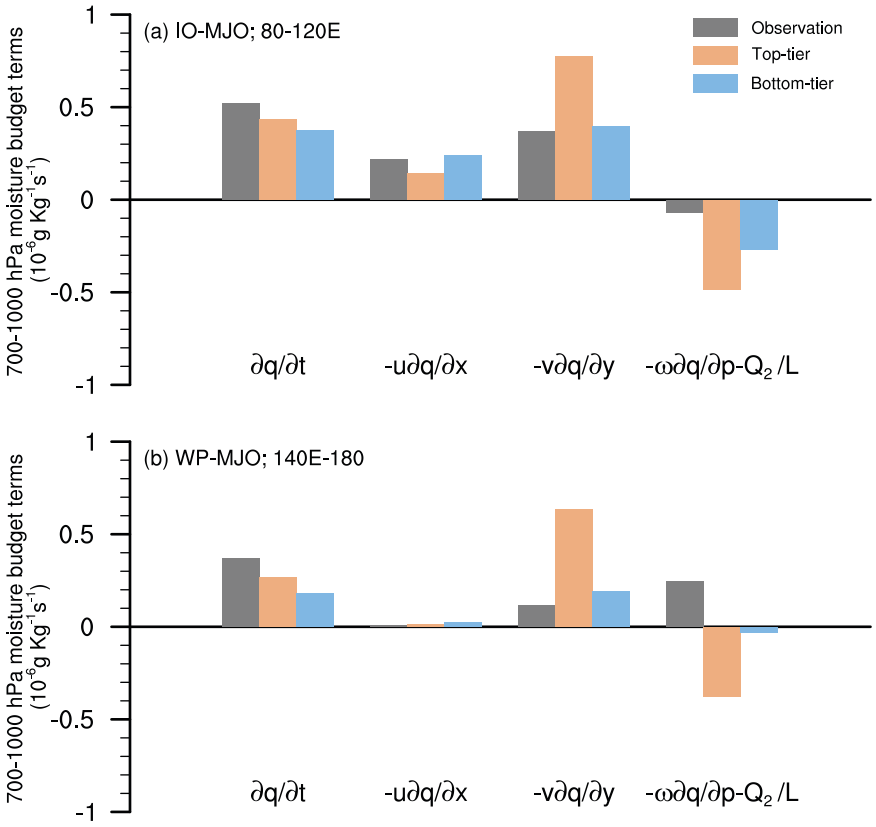

FIG. 5. Bar plots of 1000–700-hPa weight-averaged tropical (15°S–15°N averaged) moisture tendency, zonal and meridional moisture advection, and column processes (10^{-6} g kg^{-1} s^{-1}) ahead of the MJO convection center for (a) IO-MJO and (b) WP-MJO in the observations (gray bars) and the top-tier (red) and bottom-tier (blue) simulations. The values are obtained by averaging between day −15 and day −5 over 80°–120°E for IO-MJO and 140°E–180° for WP-MJO events.

simulation, which has been suggested in previous studies (Gonzalez and Jiang 2017; Kang et al. 2020). This will be further discussed in the next section.

c. *Background states and their impacts on the MJO simulation*

In this study, the background states were treated as the slowly evolving mean states under which the MJO propagates. The background states of each IO-MJO and WP-MJO event are represented by the 100-day running mean of the 1000–700-hPa mass-weighted averaged specific humidity averaged from day −15 to day −5. They were composited for the identified IO-MJO and WP-MJO events in observations and the top- and bottom-tier simulations (Fig. 7). In the top-tier simulations, there were obvious drier biases over the off-equatorial region for the background low-level moisture of IO-MJO events (Fig. 7b). This pattern leads to a stronger background meridional moisture gradient and partially explains the larger advection of LFBS specific humidity by the intraseasonal meridional winds in the top-tier simulations (Fig. 6). In the bottom-tier simulations, there are obvious drier biases over the entire tropics for the background low-level moisture of IO-MJO events compared with the observations and the top-tier simulations (Fig. 7c). The background states of WP-MJO events show similar patterns, but they are wetter over the western-central Pacific compared with the IO-MJO events in the top- and bottom-tier simulations (Figs. 7d–f). This indicates that the background states of the MJO are also related to the interannual variabilities in the models, and are not determined by the climatology solely.

The distributions of background meridional moisture gradient and MJO meridional winds were further compared (Fig. 8). In observations, the advection of background low-level moisture by the MJO meridional winds is negative over the southern Maritime Continent and northern Indian Ocean, leading to small magnitude of this term ahead of the convection center of IO-MJO events (Fig. 8a). However, the MJO meridional winds in the top-tier simulations are well collocated with the background meridional moisture gradients,

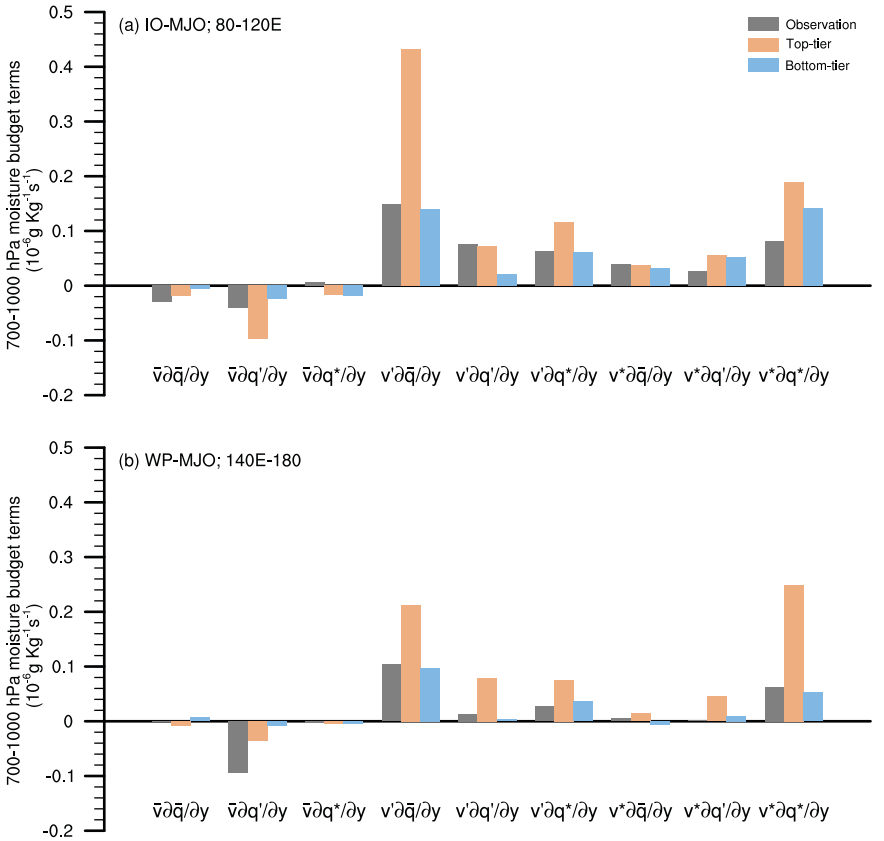

FIG. 6. As in Fig. 5, but for meridional moisture advection terms that decomposed into different time scales.

namely, southerlies under negative meridional moisture gradients and northerlies under positive meridional moisture gradients (Fig. 8b). This distribution of the MJO meridional winds, in conjunction with the larger background meridional moisture gradient, leads to larger advection of background low-level moisture by the MJO meridional wind in the top-tier simulations for IO-MJO events (Fig. 6a). For WP-MJO events, the advection of background low-level moisture by the MJO meridional winds is mainly located south of the equator in observations (Fig. 8d). But in the top-tier simulations, it is also strong over regions north of the equator (Fig. 8e). Compared with the top-tier simulations, in the bottom-tier simulations both the background meridional moisture gradient and MJO meridional winds of IO-MJO and WP-MJO events are weaker (Figs. 8c,f), leading to weaker meridional moisture advection.

Gonzalez and Jiang (2017) have suggested that mean low-level drier biases over the Maritime Continent limit the ability of the models to reproduce the MJO propagation. For both IO-MJO and WP-MJO events, there is significant intermodel correlation between their occurrence frequencies and the background low-level moisture ahead of the MJO convection among the simulations (Figs. 9a,d). Our results suggest that reducing the background low-level drier biases ahead of the MJO convection centers (eastern Indian Ocean and western Maritime Continent for IO-MJO, western Pacific for WP-MJO) plays an important role in reproducing the MJO propagation. The equatorial equatorward gradient of the background moisture ahead of the IO-MJO, defined by an averaged equatorward moisture gradient over 15°S–15°N and 80°–120°E, is significantly correlated with the annual occurrence frequencies of IO-MJO events among the models (Fig. 9b). Similar results also exist for WP-MJO events (Fig. 9e). This clearly shows that the ability of the models to reproduce the MJO propagation, as represented by the occurrence frequency of the individual MJO events, is dependent on the background meridional low-level moisture gradient ahead of the MJO convection for both IO-MJO and WP-MJO events. There is also significant intermodel correlation between the annual occurrence frequencies of IO-MJO events and the zonal moisture gradient ahead the MJO convection in the models (Fig. 9c), but no such correlation for WP-MJO events (Fig. 9f). The reason for this is that the contribution of the zonal moisture advection is negligible for the moisture accumulation ahead of the MJO convection of WP-MJO events (Fig. 5b). These results are consistent with the above moisture

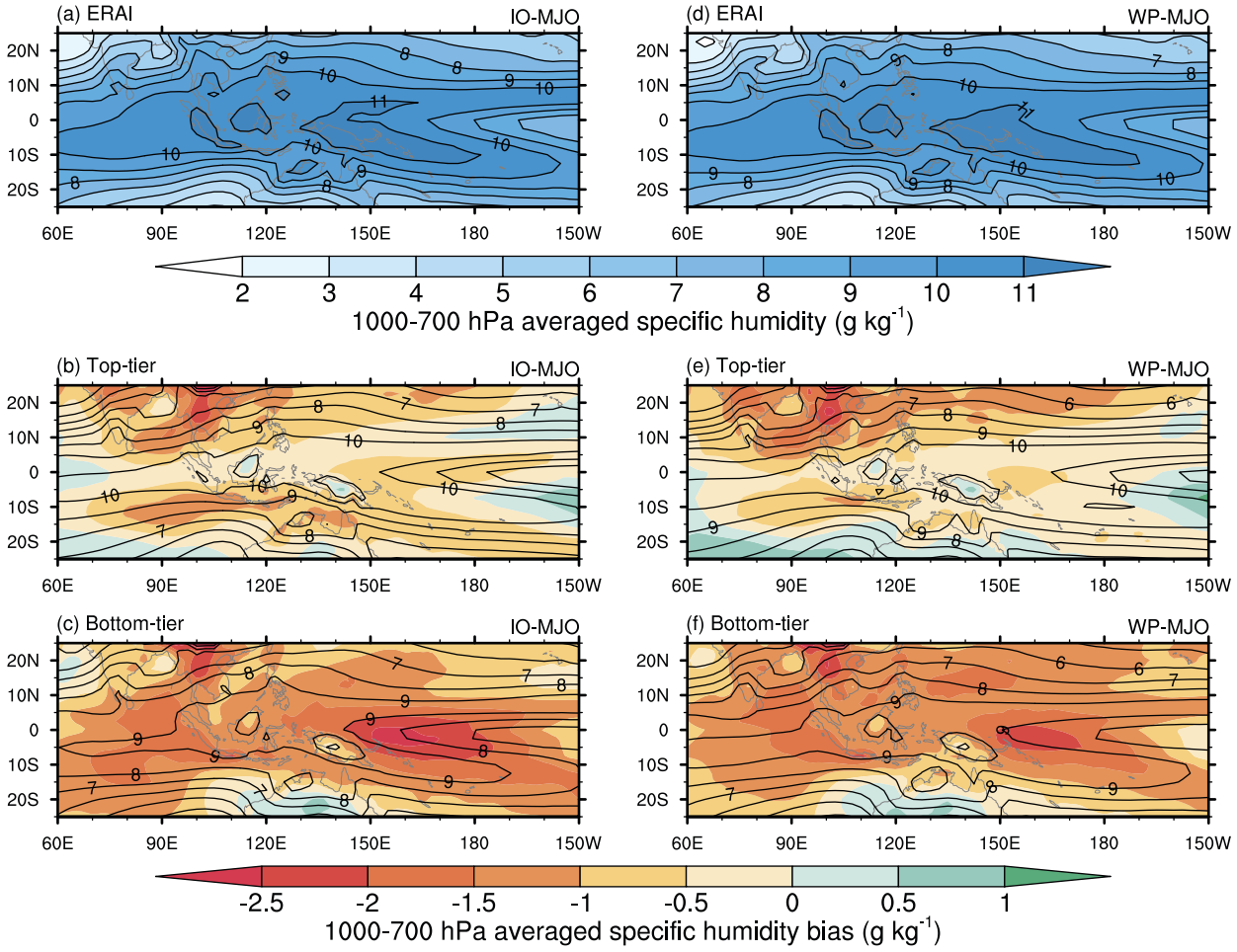

FIG. 7. Composites of 100-day running mean of 1000–700-hPa weight-averaged specific humidity (contours, with intervals of 1 g kg^{-1}) for (a)–(c) IO-MJO and (d)–(f) WP-MJO events in the (top) observations, (middle) top-tier simulations, and (bottom) bottom-tier simulations. The shadings in (b) and (c) and in (e) and (f) are the corresponding differences between the top- and bottom-tier simulations and the ERA-Interim observations.

budget analysis and previous studies (Kim et al. 2014; Kang et al. 2020).

d. Climatology and anomaly components of the background states

Ling et al. (2017) has proposed that if a model can reproduce the year-to-year background states favorable for MJO propagation more frequently, it will produce individual MJO events more frequently. The year-to-year background states of the MJO in the models, defined as the 100-day running mean of 1000–700-hPa weight-averaged specific humidity, can be decomposed into the climatology and anomaly components. The climatology components are the annual cycle of this year-to-year background states, while the anomaly components are the rest. The anomaly components can be treated as the interannual variabilities of background states. For two models producing similar climatology that is unfavorable to MJO production, if one produces larger interannual variabilities in the background states, it will tend to reproduce the year-to-year background states favorable to MJO more frequently than another model with smaller interannual variabilities. Thus, the MJO simulation in the models might not solely depend on their climatology but may also relate to the interannual variabilities of the background states. It is intriguing to explore the relative importance of climatology and the interannual variabilities of the background states on the MJO propagation in the simulations.

We first compared the boreal winter climatology of the equatorward low-level moisture gradients between the top- and bottom-tier simulations. The equatorward low-level moisture gradient is larger in the top-tier simulations over the tropical Indian Ocean and western Pacific (Fig. 10a). This is consistent with Figs. 9b and 9d, suggesting that the background equatorward low-level moisture gradient ahead of the MJO convection center is larger in the top-tier simulations. The intermodel correlation coefficients between the climatology of the equatorial averaged equatorward low-level moisture gradient and the occurrence frequencies of IO-MJO and WP-MJO events were further calculated (Figs. 10b,c). They are significant over the eastern Indian Ocean and western Maritime Continent for IO-

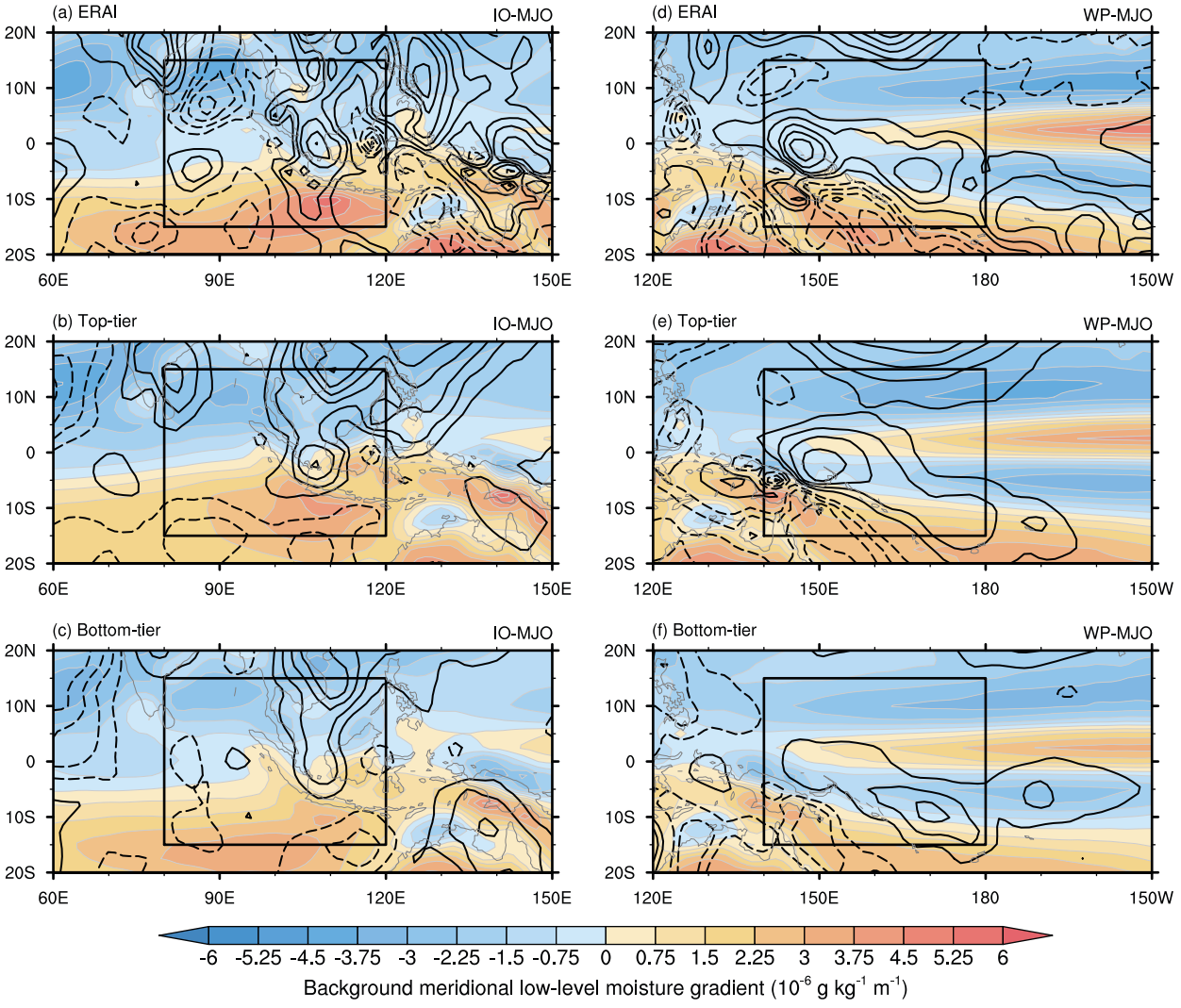

FIG. 8. Composites of 100-day running mean of meridional gradient of 1000–700-hPa weight-averaged specific humidity (shading; 10^{-6} g kg^{-1} m^{-1}) and 20–100-day bandpass filtered 850-hPa meridional wind anomalies (contours with intervals of 0.1 m s^{-1}; solid for positive values and dashed for negative values, with zero contours omitted) for (a)–(c) IO-MJO and (d)–(f) WP-MJO events in the (top) observations, (middle) top-tier simulations, and (bottom) bottom-tier simulations. The black rectangles mark the regions ahead of the MJO convection for IO-MJO (80°–120°E, 15°S–15°N) and WP-MJO events (140°E–180°, 15°S–15°N).

MJO events (Fig. 10b). The averaged correlation coefficient over regions ahead of the MJO convection centers (80°–120°E, 15°S–15°N) is 0.56, close to that between the background equatorward low-level moisture gradient and IO-MJO occurrence frequency (0.58 as shown in Fig. 9b). This suggests that the intermodel differences in the background equatorward low-level moisture gradient of IO-MJO events are mainly determined by the climatology components in the models. For WP-MJO events, the correlation is significant over the Maritime Continent and western-central Pacific (Fig. 10c), with a correlation coefficient of 0.46 over regions ahead of the MJO convection center (140°E–180°, 15°S–15°N). This correlation coefficient is lower than that of the background states (r = 0.62 as shown in Fig. 9e). This demonstrates that the intermodel differences of the background states of WP-MJO events are not solely determined by the climatology; they are also regulated by the interannual variabilities of the background states.

To quantify the relative importance of climatology components and interannual variabilities of the background states in the MJO simulation, the two-dimensional distributions of occurrence frequencies for IO-MJO and WP-MJO events in the simulations as functions of the climatology and anomaly components of the background equatorward low-level moisture gradient are presented (Fig. 11). The anomaly components are calculated for each MJO event, similar to in Figs. 9b and 9e but based on the anomalous data. The identified MJO events in all the simulations were included when obtaining the two-dimensional distributions. The climatology and anomaly components of the background equatorward low-level moisture

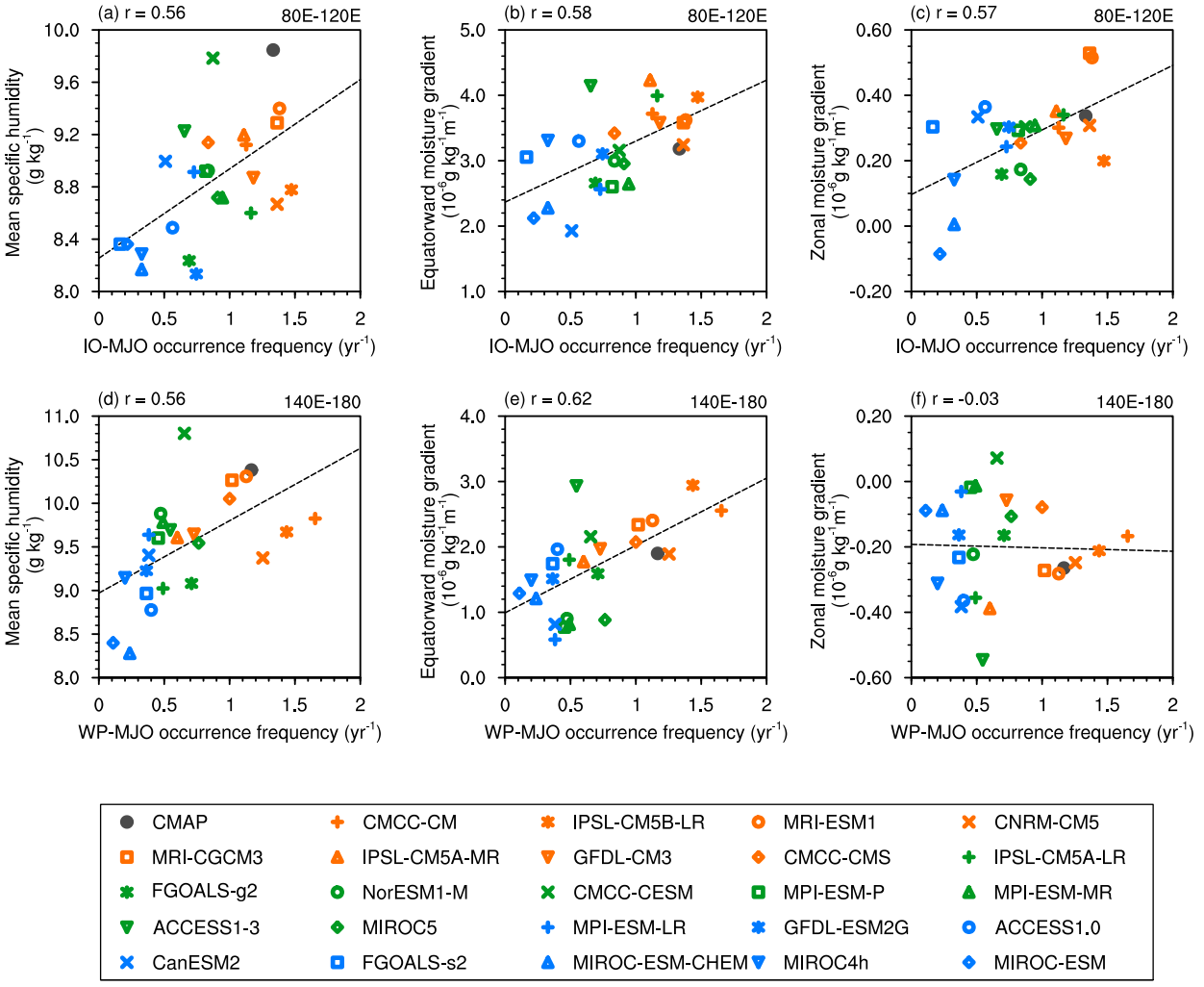

FIG. 9. Scatterplots of background states for (left) 1000–700-hPa weight-averaged specific humidity and its (center) equatorward gradient and (right) zonal gradient ahead of the MJO convection vs MJO occurrence frequencies (yr^{-1}) for (a)–(c) IO-MJO and (d)–(f) WP-MJO events. The values in the *y* axis were obtained by averaging over 15°S–15°N, 80°–120°E for IO-MJO and over 15°S–15°N, 140°E–180° for WP-MJO.

gradient in each simulation are also provided in Fig. 11, indicated by the black dots. There are obvious year-to-year variations of the anomaly components in background equatorward low-level moisture gradient related with both IO-MJO and WP-MJO events. But there is no obvious preference of the IO-MJO events for the anomaly components in the simulations, as their occurrence frequencies are almost symmetrically distributed along the *y* axis (Fig. 11a). In contrast, the WP-MJO events tend to occur during years under larger equatorward low-level moisture gradient (Fig. 11b). More interestingly, models that produce smaller climatology components in equatorward low-level moisture gradient tend to produce WP-MJO with larger anomaly component (Fig. 11b). These results demonstrate that the MJO propagation over the western Pacific is obviously regulated by the interannual variations of the background states. Models with larger climatology components tend to exhibit favorable background states for the WP-MJO events more frequently, and they produce WP-MJO events more frequently. In contrast, models with smaller climatology components tend to exhibit favorable background states for the WP-MJO events less frequently, and they tend to only produce WP-MJO events during boreal winters when the equatorward low-level moisture gradient is anomalous large over the western-central Pacific.

ENSO is the dominant mode of interannual variability over the tropics and has direct impacts on the year-to-year background states over the tropics. The year-to-year variations of the background horizontal low-level moisture gradients associated with ENSO were compared in observations and the simulations (Fig. 12). The dots denote the values of the low-level moisture gradients anomalies and Niño-3.4 SST anomalies that calculated by averaging for each boreal winter season in observations, while the red crosses represent the values in the 24 simulations evaluated in this study. Over the eastern Indian Ocean and western Maritime Continent (80°–120°E),

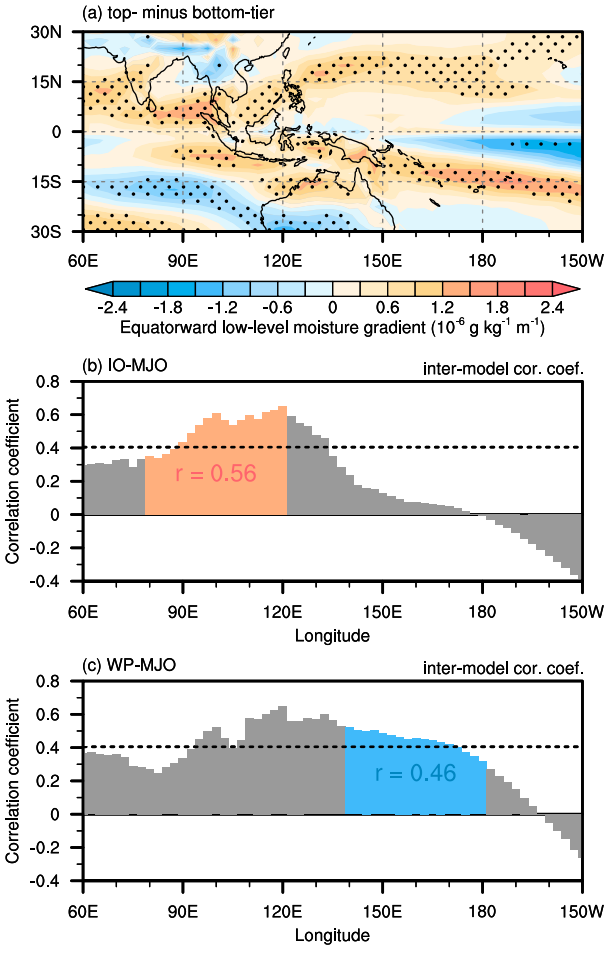

FIG. 10. (a) Differences in climatology of equatorward gradient for 1000–700-hPa weight-averaged specific humidity (g kg^{-1} m^{-1}) between the top- and bottom-tier simulations and intermodel correlation coefficients of occurrence frequencies of (b) IO-MJO and (c) WP-MJO events with 15°S–15°N averaged climatology in equatorward gradients of the 1000–700-hPa weight-averaged specific humidity among the simulations during boreal winter. The orange and blue bars in (b) and (c) mark the regions ahead of the MJO convection centers, with the correlation coefficient presented. The dotted lines mark the correlation coefficient at the 95% confidence level.

the equatorward moisture gradient increases as the Niño-3.4 SST increases; the linear regression coefficient is 0.3 in the observations but only 0.24 in the simulations (Fig. 12a). The underestimated regression coefficient by 20% in the simulations suggests that the ENSO impacts on the equatorward moisture gradient are underestimated by about 20% over this region in the simulations. Over this region, unlike the equatorward moisture gradient, the zonal moisture gradient decreases as the Niño-3.4 SST increases (Fig. 12c). The ENSO impacts on the zonal moisture gradient tend to offset its impacts on the equatorward moisture gradient. Results in section 3b suggest that the zonal moisture advection over the Indian Ocean is also important for the MJO propagation. In this case, the opposite impacts of ENSO on the zonal and equatorward moisture gradients lead to no obvious impacts of anomaly components of the background states on IO-MJO events. Moreover, ENSO impacts on zonal moisture gradient over the eastern Indian Ocean and western Maritime Continent are underestimated by about 60% in the simulations, as the regression coefficient is −0.1 in observations and −0.04 in the simulations (Fig. 12c). Over the western Pacific (Figs. 12b,d), both the equatorward and zonal low-level moisture gradients increase as the Niño-3.4 SST increases. This suggests that the background states in equatorward and zonal low-level moisture gradients during El Niño are favorable for MJO propagation over the western Pacific. This is consistent with results that suggest El Niño is more favorable for MJO activities over the Pacific, which has been shown by previous studies (Li and Smith 1995; Tam and Lau 2005; Wu and Song 2018; Wei and Ren 2019; B. Wang et al. 2019; Chen and Wang 2020).

We further compared the impacts of ENSO on the background states in observations and the simulations by identifying the ENSO events. For each boreal winter season, if the normalized seasonal mean Niño-3.4 SST anomaly exceeds 0.5, it is treated as an El Niño winter; and if it is less than −0.5, it is then defined as an La Niña winter. In observations, there are 12 El Niño and 12 La Niña winters identified. Figure 13 shows the differences in boreal winter mean 1000–700-hPa weight-averaged specific humidity and SST between El Niño and La Niña winters in observations and the simulations. In observations, during El Niño winters, the low-level troposphere is wetter over the western-central Pacific and western Indian Ocean, and drier over the Maritime Continent and its off-equatorial regions (Fig. 13a). This leads to reduced background zonal moisture gradient and enhanced background equatorward moisture gradient during El Niño over the eastern Indian Ocean and western Maritime Continent, as shown in Fig. 12. But both equatorward and zonal moisture gradients over the western Pacific Ocean are larger during El Niño than during La Niña in the observation. This leads to more WP-MJO events occurring during El Niño in both observations and the simulations. The distribution of moisture differences is assembling with warmer SST anomalies over the central-eastern Pacific and western Indian Ocean, colder SST anomalies over the eastern Maritime Continent and western Pacific (Fig. 13c). The ENSO impacts on the background states in the simulations are different (Figs. 13b,d). The wetter low-level moisture anomalies and warmer SST anomalies over the tropical Pacific extend farther west compared with observations (Figs. 13b,d). As a result, the drier low-level moisture anomalies over the equatorial region of the Maritime Continent during El Niño are not so obvious in the simulations (Fig. 13b). This leads to obvious decreased impacts of ENSO on the zonal moisture gradient over the eastern Indian Ocean and western Maritime Continent in the simulations. This might be related to the excessive westward extension of ENSO variability and the excessive cold tongue biases in the simulations (Li and Xie 2014; Kug et al. 2012; Jiang et al. 2021).

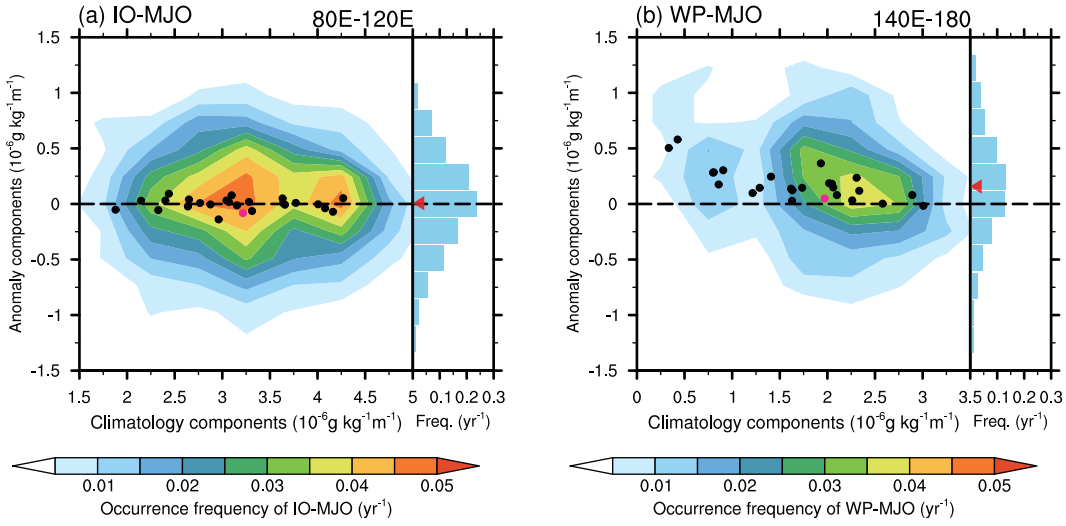

FIG. 11. Joint distributions of occurrence frequencies (yr^{-1}) of (a) IO-MJO and (b) WP-MJO events as functions of the anomaly components (y axis; 10^{-6} g kg^{-1} m^{-1}) and climatology components (x axis; 10^{-6} g kg^{-1} m^{-1}) of their corresponding background equatorward gradient of 1000–700-hPa weight-averaged specific humidity averaged ahead of the MJO convection center (15°S–15°N, 80°–120°E for IO-MJO; 15°S–15°N, 140°E–180° for WP-MJO) in the 24 simulations diagnosed. The attached bar plots on the y axis are the corresponding one-dimensional distributions of MJO occurrence frequencies as functions of the anomalous equatorward moisture gradients; the red triangles mark the mean values. The black dot denotes the mean for each simulation while the magenta dot represents the observations.

4. Summary and discussion

By identifying individual MJO events, we examined the ability of 24 CMIP5 models to reproduce the MJO propagation over the Indian Ocean (IO-MJO) and western Pacific (WP-MJO), and we explored the impacts of background states on the MJO propagation. The annual occurrence frequency of individual MJO events was used to quantify how well the models can reproduce the MJO propagation, as this metric is significantly correlated with the ability of the models to reproduce the MJO statistical signals. Low-level moisture budget analysis was further applied to IO-MJO and WP-MJO events to explore the possible role of the background states on the MJO simulation. It was found that the meridional moisture advection dominates the moisture transport processes for both IO-MJO and WP-MJO events. Models that produce MJO events more frequently exhibit a stronger low-level moisture tendency ahead of the MJO convection compared with those that produce MJO events less frequently. These differences are caused by the meridional moisture advection. Scale decomposition analysis further revealed that the differences are mainly caused by the meridional advection of the background low-level moisture via the intraseasonal winds. The annual occurrence frequencies of IO-MJO and WP-MJO events in the models are determined by their background equatorward low-level moisture gradients over the Indian Ocean and western Pacific, respectively.

The background states were further decomposed into the climatology and anomaly components. In the simulations, the background equatorward moisture gradients ahead of the MJO convection centers for IO-MJO events are mainly determined by their climatology components. While they are also related to interannual variabilities of background states regulated by ENSO for WP-MJO events. Models with a climatology of warmer SST over the Niño-3.4 region tend to produce WP-MJO more frequently, while models with colder SST climatology tend to produce WP-MJO less frequently only during El Niño years. It was found that the ENSO impacts on zonal and equatorward gradient tend to offset each other on MJO propagation over the Indian Ocean. This leads to no obvious regulation of the year-to-year variations of the background states on the MJO propagation over the Indian Ocean. Both the zonal and equatorward moisture gradients are larger during El Niño than during La Niña over the western Pacific. Thus, the WP-MJO events are more likely occurred during El Niño in both observations and the simulations.

In this study, the cover period of the simulations (1950–2005) is longer than observations (1979–2015). We have reproduced the results using a common period (1979–2005) for the simulations and observations, and the results remained similar. There are also uncertainties among different observational datasets (Ahn et al. 2020; Ren et al. 2021), and one might be concerned that MJO tracking results based on the interpolated pentad CMAP precipitation are not reliable. We tried to reproduce the results using daily precipitation of the Precipitation Estimation from Remotely Sensed Information using Artificial Neural Networks–Climate Data Record (PERSIANN-CDR; Ashouri et al. 2015) from 1983 to 2015 and Tropical Rainfall Measuring Mission (TRMM) 3B42 version 7 Multisatellite Precipitation Analysis (TMPA;

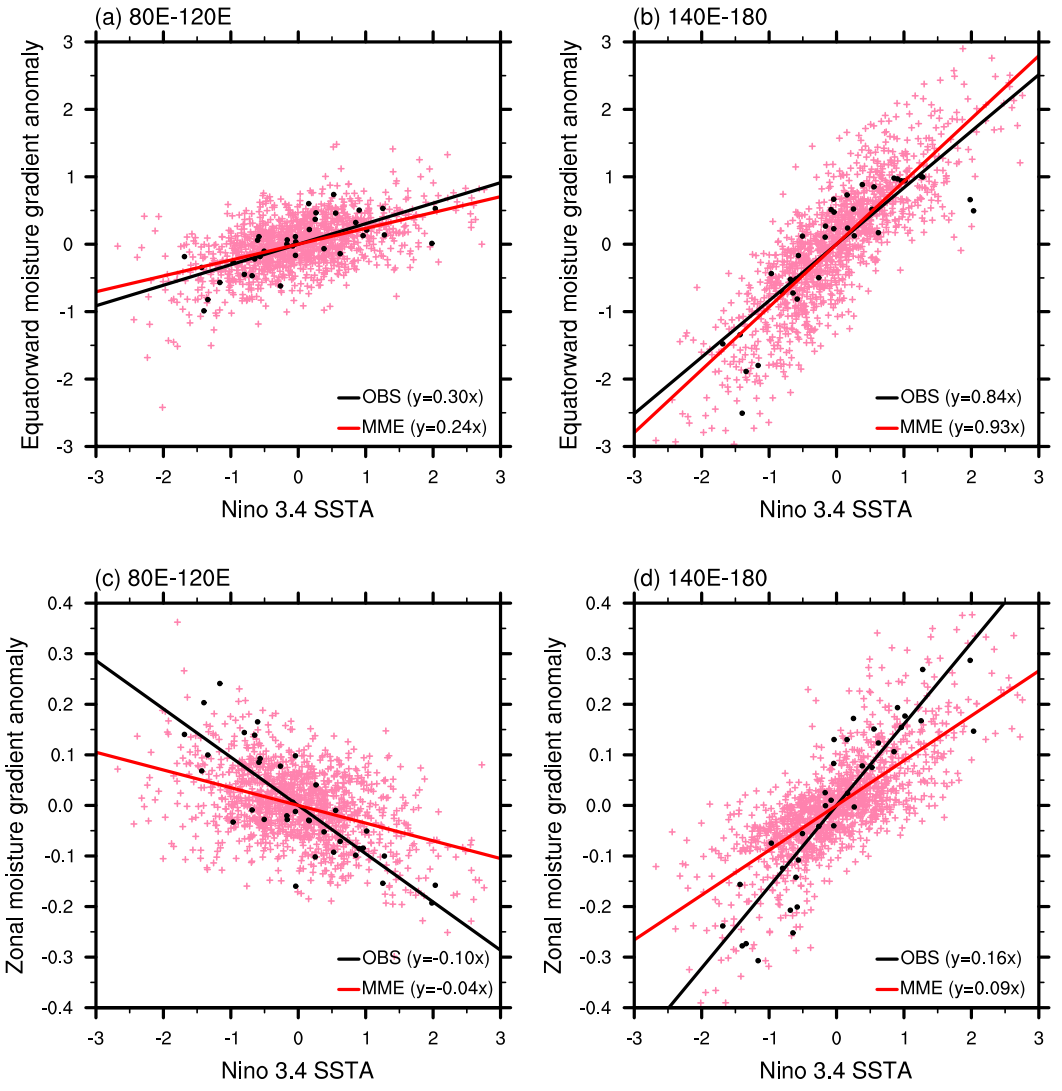

FIG. 12. Scatterplots of boreal winter mean Niño-3.4 SST anomalies (°C) differences between El Niño and La Niña years for (a) IO-MJO events and (b) WP-MJO events in the observation and the simulations. The gray bar represents the observations, the light blue bars represent the simulations, and the red bar represents the multimodel ensemble mean, with the range of one standard deviation for the simulations marked by the vertical black line.

Huffman et al. 2007) from 1998 to 2015; the composites for the identified MJO events and their background states remained similar.

This study highlights the importance of year-to-year background states on the MJO in climate model simulations. Apart from ENSO, the quasi-biennial oscillation (QBO) is the dominant mode of interannual variability over the tropics (Baldwin et al. 2001). The MJO propagation is significantly modulated by the QBO (Son et al. 2017). It has also been suggested that ENSO and QBO have combined effects on the MJO (Sun et al. 2019). Specifically, the MJO might also propagate a long distance during La Niña years if it is also under the QBO easterly phase. As most of the current climate models cannot reproduce the QBO, it is unlikely they can reproduce the QBO–MJO connection. Thus, the underestimation in occurrence frequency of MJO when the Niño-3.4 SSTA is under −1°C in the simulations might be a result of lacking QBO effects on MJO propagation in the simulations, as has been suggested currently (Lim et al. 2019; S. Wang et al. 2019; Kim et al. 2020). It is necessary to study the interannual variabilities of MJO that related to the QBO in the climate models based on the diagnosis method proposed in this study.

This study also highlights the importance of reproducing the SST over the equatorial Pacific region for improved MJO simulation. However, it does not mean that the top-tier simulations can produce realistic background states globally. Higher occurrence frequency of MJO events in the top-tier simulations might the result of error compensation. The low-level drier biases over the off-equatorial region in the top-tier simulations, which lead to stronger background equatorward

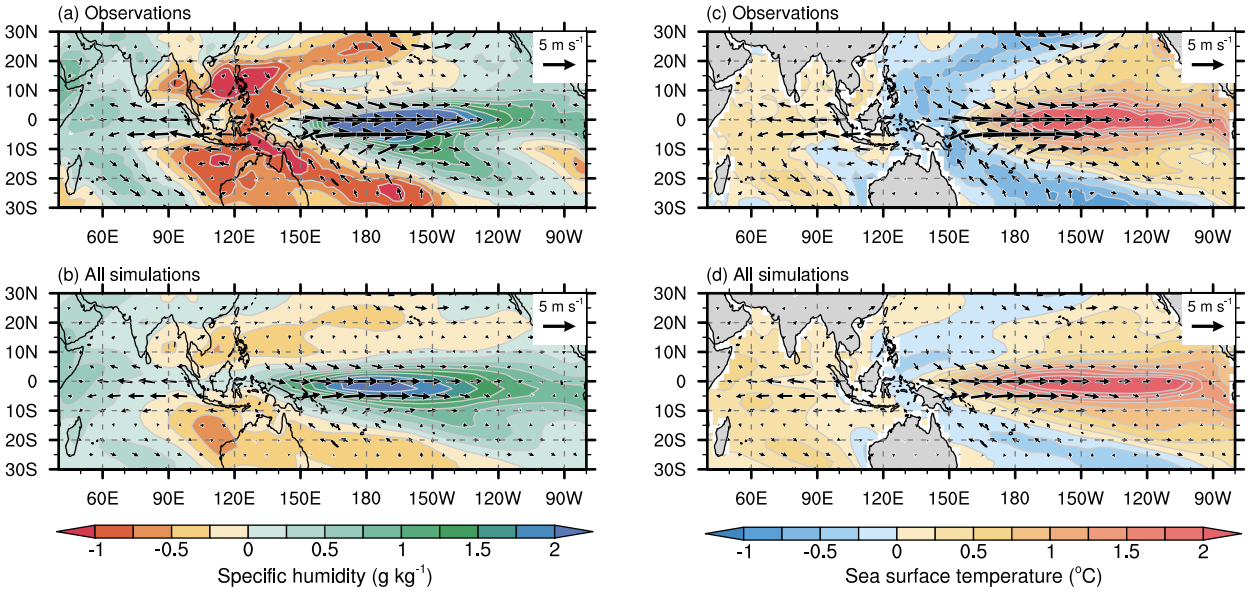

FIG. 13. Horizontal distributions of the differences in boreal winter mean 1000–700-hPa weight-averaged (a),(b) specific humidity (g kg^{-1}) and (c),(d) SST (°C) and the corresponding 850-hPa horizontal winds (vectors; m s^{-1}) between El Niño and La Niña (El Niño minus La Niña) in (top) observations and (bottom) all simulations.

moisture gradient over the equatorial region. This background states further promotes the MJO propagation in the top-tier simulations. There are also stronger warm biases in the boreal winter mean SST over the southern eastern Pacific. Thus, when we use the observed initial conditions to derive real-time MJO prediction in the top-tier simulations, the skill might be low (Ling et al. 2017). Further studies exploring the sources of background state biases are needed because the MJO simulation in climate models needs to be improved under the right background states.

Acknowledgments. This research was sponsored by the National Key R&D Program of China through Grants 2018YFC1505901 and 2018YFA0606203, the National Nature Science Foundation of China through Grants 41922035, 41575062, and 41520104008, the Key Research Program of Frontier Sciences of CAS through Grant QYZDB-SSW-DQC017, the State Key Laboratory of Tropical Oceanography, the South China Sea Institute of Oceanology, and the Chinese Academy of Sciences (Project LTO2004). Xin Wang was supported by the Strategic Priority Research Program of Chinese Academy of Sciences (Grant XDB42000000), the National Natural Science Foundation of China (Grant 41925024), and the Key Special Project for Introduced Talents Team of Southern Marine Science and Engineering Guangdong Laboratory (Guangzhou) (GML2019ZD0306).

REFERENCES

Adames, Á. F., and J. M. Wallace, 2015: Three-dimensional structure and evolution of the moisture field in the MJO. *J. Atmos. Sci.*, **72**, 3733–3754, https://doi.org/10.1175/JAS-D-15-0003.1.

Ahn, M.-S., and Coauthors, 2020: MJO propagation across the Maritime Continent: Are CMIP6 models better than CMIP5 models? *Geophys. Res. Lett.*, **47**, e2020GL087250, https://doi.org/10.1029/2020GL087250.

Ashouri, H., K.-L. Hsu, S. Sorooshian, D. K. Braithwaite, K. R. Knapp, L. D. Cecil, B. R. Nelson, and O. P. Prat, 2015: PERSIANN-CDR: Daily precipitation climate data record from multisatellite observations for hydrological and climate studies. *Bull. Amer. Meteor. Soc.*, **96**, 69–83, https://doi.org/10.1175/BAMS-D-13-00068.1.

Baldwin, M. P., and Coauthors, 2001: The quasi-biennial oscillation. *Rev. Geophys.*, **39**, 179–229, https://doi.org/10.1029/1999RG000073.

Chen, G. S., and B. Wang, 2020: Circulation factors determining the propagation speed of the Madden–Julian oscillation. *J. Climate*, **33**, 3367–3380, https://doi.org/10.1175/JCLI-D-19-0661.1.

Chen, G. W., J. Ling, C. Li, Y. Zhang, and C. Zhang, 2020: Barrier effect of the Indo-Pacific Maritime Continent on MJO propagation in observations and CMIP5 models. *J. Climate*, **33**, 5173–5193, https://doi.org/10.1175/JCLI-D-19-0771.1.

Dee, D. P., and Coauthors, 2011: The ERA-Interim reanalysis: Configuration and performance of the data assimilation system. *Quart. J. Roy. Meteor. Soc.*, **137**, 553–597, https://doi.org/10.1002/qj.828.

Gonzalez, A. O., and X. Jiang, 2017: Winter mean lower tropospheric moisture over the Maritime Continent as a climate model diagnostic metric for the propagation of the Madden–Julian oscillation. *Geophys. Res. Lett.*, **44**, 2588–2596, https://doi.org/10.1002/2016GL072430.

Gottschalck, J., P. E. Roundy, C. J. Schreck, A. Vintzileos, and C. D. Zhang, 2013: Large-scale atmospheric and oceanic conditions during the 2011–12 DYNAMO field campaign. *Mon. Wea. Rev.*, **141**, 4173–4196, https://doi.org/10.1175/MWR-D-13-00022.1.

Hsu, P.-C., and T. Li, 2012: Role of the boundary layer moisture asymmetry in causing the eastward propagation of the Madden–Julian oscillation. *J. Climate*, **25**, 4914–4931, https://doi.org/10.1175/JCLI-D-11-00310.1.

——, ——, and H. Murakami, 2014: Moisture asymmetry and MJO eastward propagation in an aquaplanet general circulation model. *J. Climate*, **27**, 8747–8760, https://doi.org/10.1175/JCLI-D-14-00148.1.

Huffman, G. J., and Coauthors, 2007: The TRMM Multisatellite Precipitation Analysis (TMPA): Quasi-global, multiyear, combined-sensor precipitation estimates at fine scales. *J. Hydrometeor.*, **8**, 38–55, https://doi.org/10.1175/JHM560.1.

Hung, M., J. Lin, W. Wang, D. Kim, T. Shinoda, and S. J. Weaver, 2013: MJO and convectively coupled equatorial waves simulated by CMIP5 climate models. *J. Climate*, **26**, 6185–6214, https://doi.org/10.1175/JCLI-D-12-00541.1.

Inness, P. M., and J. M. Slingo, 2003: Simulation of the Madden–-Julian oscillation in a coupled general circulation model. Part I: Comparisons with observations and an atmosphere-only GCM. *J. Climate*, **16**, 345–364, https://doi.org/10.1175/1520-0442(2003)016<0345:SOTMJO>2.0.CO;2.

——, ——, E. Guilyardi, and J. Cole, 2003: Simulation of the Madden–Julian oscillation in a coupled general circulation model. Part II: The role of the basic state. *J. Climate*, **16**, 365–382, https://doi.org/10.1175/1520-0442(2003)016<0365:SOTMJO>2.0.CO;2.

Jia, X., C. Li, J. Ling, and C. Zhang, 2008: Impacts of a GCM's resolution on MJO simulation. *Adv. Atmos. Sci.*, **25**, 139–156, https://doi.org/10.1007/s00376-008-0139-9.

Jiang, W., P. Huang, G. Huang, and J. Ying, 2021: Origins of the excessive westward extension of ENSO SST simulated in CMIP5 and CMIP6 models. *J. Climate*, **34**, 2839–2851, https://doi.org/10.1175/JCLI-D-20-0551.1.

Jiang, X., and Coauthors, 2015: Vertical structure and physical processes of the Madden–Julian oscillation: Exploring key model physics in climate simulations. *J. Geophys. Res. Atmos.*, **120**, 4718–4748, https://doi.org/10.1002/2014JD022375.

Kang, D., D. Kim, M.-S. Ahn, R. Neale, J. Lee, and P. J. Gleckler, 2020: The role of the mean state on MJO simulation in CESM2 ensemble simulation. *Geophys. Res. Lett.*, **47**, e2020GL089824, https://doi.org/10.1029/2020GL089824.

Kim, D., and Coauthors, 2009: Application of MJO simulation diagnostics to climate models. *J. Climate*, **22**, 6413–6436, https://doi.org/10.1175/2009JCLI3063.1.

——, J. S. Kug, and A. H. Sobel, 2014: Propagating versus nonpropagating Madden–Julian oscillation events. *J. Climate*, **27**, 111–125, https://doi.org/10.1175/JCLI-D-13-00084.1.

——, F. Vitart, and D. E. Waliser, 2018: Prediction of the Madden–Julian oscillation: A review. *J. Climate*, **31**, 9425–9443, https://doi.org/10.1175/JCLI-D-18-0210.1.

——, J. M. Caron, J. H. Richter, and I. R. Simpson, 2020: The lack of QBO-MJO connection in CMIP6 models. *Geophys. Res. Lett.*, **47**, e2020GL087295, https://doi.org/10.1029/2020GL087295.

Kim, H.-M., 2017: The impact of the mean moisture bias on the key physics of MJO propagation in the ECMWF reforecast. *J. Geophys. Res. Atmos.*, **122**, 7772–7784, https://doi.org/10.1002/2017JD027005.

Kiranmayi, L., and E. D. Maloney, 2011: Intraseasonal moist static energy budget in reanalysis data. *J. Geophys. Res.*, **116**, D21117, https://doi.org/10.1029/2011JD016031.

Klingaman, N. P., and C. A. Demott, 2020: Mean state biases and interannual variability affect perceived sensitivities of the Madden–Julian oscillation to air–sea coupling. *J. Adv. Model. Earth Syst.*, **12**, e2019MS001799, https://doi.org/10.1029/2019MS001799.

Kug, J.-S., Y.-G. Ham, J.-Y. Lee, and F.-F. Jin, 2012: Improved simulation of two types of El Niño in CMIP5 models. *Environ. Res. Lett.*, **7**, 034002, https://doi.org/10.1088/1748-9326/7/3/034002.

Li, C., and I. Smith, 1995: Numerical simulation of the tropical intraseasonal oscillation and the effect of warm SST. *J. Meteor. Res.*, **9**, 1–12, http://jmr.cmsjournal.net/en/article/id/533?articleType=archive_en.

Li, G., and S. Xie, 2014: Tropical biases in CMIP5 multimodel ensemble: The excessive equatorial Pacific cold tongue and double ITCZ problems. *J. Climate*, **27**, 1765–1780, https://doi.org/10.1175/JCLI-D-13-00337.1.

Li, T., J. Ling, and P.-C. Hsu, 2020: Madden–Julian Oscillation: Its discovery, dynamics, and impact on East Asia. *J. Meteor. Res.*, **34**, 20–42, https://doi.org/10.1007/s13351-020-9153-3.

Lim, Y., S.-W. Son, A. G. Marshall, H. H. Hendon, and K.-H. Seo, 2019: Influence of the QBO on MJO prediction skill in the subseasonal-to-seasonal prediction models. *Climate Dyn.*, **53**, 1681–1695, https://doi.org/10.1007/s00382-019-04719-y.

Ling, J., C. Li, and X. Jia, 2009: Impacts of cumulus momentum transport on MJO simulation. *Adv. Atmos. Sci.*, **26**, 864–876, https://doi.org/10.1007/s00376-009-8016-8.

——, P. Bauer, P. Bechtold, A. Beljaars, R. Forbes, F. Vitart, M. Ulate, and C. Zhang, 2014: Global versus local MJO forecast skill of the ECMWF model during DYNAMO. *Mon. Wea. Rev.*, **142**, 2228–2247, https://doi.org/10.1175/MWR-D-13-00292.1.

——, C. Zhang, S. Wang, and C. Li, 2017: A new interpretation of the ability of global models to simulate the MJO. *Geophys. Res. Lett.*, **44**, 5798–5806, https://doi.org/10.1002/2017GL073891.

——, Y. Zhao, and G. Chen, 2019: Barrier effect on MJO propagation by the Maritime Continent in the MJO Task Force/GEWEX atmospheric system study models. *J. Climate*, **32**, 5529–5547, https://doi.org/10.1175/JCLI-D-18-0870.1.

Liu, F., L. Zhou, J. Ling, X. Fu, and G. Huang, 2016: Relationship between SST anomalies and the intensity of intraseasonal variability. *Theor. Appl. Climatol.*, **124**, 847–854, https://doi.org/10.1007/s00704-015-1458-2.

Liu, J., Y. Da, T. Li, and F. Hu, 2020: Impact of ENSO on MJO pattern evolution over the Maritime Continent. *J. Meteor. Res.*, **34**, 1151–1166, https://doi.org/10.1007/s13351-020-0046-2.

Liu, P., Q. Zhang, C. Zhang, Y. Zhu, M. Khairoutdinov, H. M. Kim, C. Schumacher, and M. Zhang, 2016: A revised real-time multivariate MJO index. *Mon. Wea. Rev.*, **144**, 627–642, https://doi.org/10.1175/MWR-D-15-0237.1.

Madden, R. A., and P. R. Julian, 1971: Detection of a 40–50-day oscillation in zonal wind in tropical Pacific. *J. Atmos. Sci.*, **28**, 702–708, https://doi.org/10.1175/1520-0469(1971)028<0702:DOADOI>2.0.CO;2.

——, and ——, 1972: Description of global-scale circulation cells in tropics with a 40–50 day period. *J. Atmos. Sci.*, **29**, 1109–1123, https://doi.org/10.1175/1520-0469(1972)029<1109:DOGSCC>2.0.CO;2.

Maloney, E. D., 2009: The moist static energy budget of a composite tropical intraseasonal oscillation in a climate model. *J. Climate*, **22**, 711–729, https://doi.org/10.1175/2008JCLI2542.1.

Pang, B., R. Lu, and J. Ling, 2018: Impact of cold surges on the Madden–Julian Oscillation propagation over the Maritime

Continent. *Atmos. Sci. Lett.*, **19**, e854, https://doi.org/10.1002/asl.854.

Rayner, N. A., and Coauthors, 2003: Global analyses of sea surface temperature, sea ice, and night marine air temperature since the late nineteenth century. *J. Geophys. Res.*, **108**, 4407, https://doi.org/10.1029/2002JD002670.

Ren, P., D. Kim, M. Ahn, D. Kang, and H. Ren, 2021: Intercomparison of MJO column moist static energy and water vapor budget among six modern reanalysis products. *J. Climate*, **34**, 2977–3001, https://doi.org/10.1175/JCLI-D-20-0653.1.

Seo, K., J. E. Schemm, W. Wang, and A. Kumar, 2007: The boreal summer intraseasonal oscillation simulated in the NCEP Climate Forecast System: The effect of sea surface temperature. *Mon. Wea. Rev.*, **135**, 1807–1827, https://doi.org/10.1175/MWR3369.1.

Son, S.-W., Y. Lim, C. Yoo, H. H. Hendon, and J. Kim, 2017: Stratospheric control of the Madden–Julian oscillation. *J. Climate*, **30**, 1909–1922, https://doi.org/10.1175/JCLI-D-16-0620.1.

Sperber, K. R., 2004: Madden–Julian variability in NCAR CAM2.0 and CCSM2.0. *Climate Dyn.*, **23**, 259–278, https://doi.org/10.1007/s00382-004-0447-4.

Straub, K. H., 2013: MJO initiation in the real-time multivariate MJO index. *J. Atmos. Sci.*, **26**, 1130–1151, https://doi.org/10.1175/JCLI-D-12-00074.1.

Sun, L., H. Wang, and F. Liu, 2019: Combined effect of the QBO and ENSO on the MJO. *Atmos. Oceanic Sci. Lett.*, **12**, 170–176, https://doi.org/10.1080/16742834.2019.1588064.

Tam, C. Y., and N. C. Lau, 2005: Modulation of the Madden–Julian Oscillation by ENSO: Inferences from observations and GCM simulations. *J. Meteor. Soc. Japan*, **83**, 727–743, https://doi.org/10.2151/jmsj.83.727.

Taylor, K. E., R. J. Stouffer, and G. A. Meehl, 2012: An overview of CMIP5 and the experiment design. *Bull. Amer. Meteor. Soc.*, **93**, 485–498, https://doi.org/10.1175/BAMS-D-11-00094.1.

Wang, B., and Coauthors, 2018: Dynamics-oriented diagnostics for the Madden–Julian oscillation. *J. Climate*, **31**, 3117–3135, https://doi.org/10.1175/JCLI-D-17-0332.1.

——, G. Chen, and F. Liu, 2019: Diversity of the Madden–Julian Oscillation. *Sci. Adv.*, **5**, eaax0220, https://doi.org/10.1126/sciadv.aax0220.

Wang, S., M. K. Tippett, A. H. Sobel, Z. Martin, and F. Vitart, 2019: Impact of the QBO on prediction and predictability of the MJO convection. *J. Geophys. Res. Atmos.*, **124**, 11 766–11 782, https://doi.org/10.1029/2019JD030575.

Wei, Y. T., and H. L. Ren, 2019: Modulation of ENSO on fast and slow MJO modes during boreal winter. *J. Climate*, **32**, 7483–7506, https://doi.org/10.1175/JCLI-D-19-0013.1.

Wheeler, M. C., and G. N. Kiladis, 1999: Convectively coupled equatorial waves: Analysis of clouds and temperature in the wavenumber–frequency domain. *J. Atmos. Sci.*, **56**, 374–399, https://doi.org/10.1175/1520-0469(1999)056<0374:CCEWAO>2.0.CO;2.

——, and H. H. Hendon, 2004: An all-season real-time multivariate MJO index: Development of an index for monitoring and prediction. *Mon. Wea. Rev.*, **132**, 1917–1932, https://doi.org/10.1175/1520-0493(2004)132<1917:AARMMI>2.0.CO;2.

Wu, R., and L. Song, 2018: Spatiotemporal change of intraseasonal oscillation intensity over the tropical Indo-Pacific Ocean associated with El Niño and La Niña events. *Climate Dyn.*, **50**, 1221–1242, https://doi.org/10.1007/s00382-017-3675-0.

Xie, P., and P. A. Arkin, 1997: Global precipitation: A 17-year monthly analysis based on gauge observations, satellite estimates, and numerical model outputs. *Bull. Amer. Meteor. Soc.*, **78**, 2539–2558, https://doi.org/10.1175/1520-0477(1997)078<2539:GPAYMA>2.0.CO;2.

Yanai, M., S. Esbensen, and J.-H. Chu, 1973: Determination of bulk properties of tropical cloud clusters from large-scale heat and moisture budgets. *J. Atmos. Sci.*, **30**, 611–627, https://doi.org/10.1175/1520-0469(1973)030<0611:DOBPOT>2.0.CO;2.

Zhang, C., 2005: Madden–Julian Oscillation. *Rev. Geophys.*, **43**, RG2003, https://doi.org/10.1029/2004RG000158.

——, 2013: Madden–Julian oscillation: Bridging weather and climate. *Bull. Amer. Meteor. Soc.*, **94**, 1849–1870, https://doi.org/10.1175/BAMS-D-12-00026.1.

——, and H. H. Hendon, 1997: Propagating and stationary components of the intraseasonal oscillation in tropical convection. *J. Atmos. Sci.*, **54**, 741–767, https://doi.org/10.1175/1520-0469(1997)054<0741:PASCOT>2.0.CO;2.

——, and J. Ling, 2017: Barrier effect of the Indo-Pacific Maritime Continent on the MJO: Perspectives from tracking MJO precipitation. *J. Climate*, **30**, 3439–3459, https://doi.org/10.1175/JCLI-D-16-0614.1.

——, and Coauthors, 2006: Simulations of the Madden–Julian Oscillation by four pairs of coupled and uncoupled global models. *Climate Dyn.*, **27**, 573–592, https://doi.org/10.1007/s00382-006-0148-2.

Zhao, C. B., T. Li, and T. J. Zhou, 2013: Precursor signals and processes associated with MJO initiation over the tropical Indian Ocean. *J. Climate*, **26**, 291–307, https://doi.org/10.1175/JCLI-D-12-00113.1.